

ET-NE 98-02
ISBN 87-7475-192-1

DK 9801372

January 1998

MASTER

Basic Rotor Aerodynamics applied to Wind Turbines

Martin O.L.Hansen

RECEIVED
JUN 25 1998
OSTI



Department of Energy Engineering
Fluid Mechanics

Technical University of Denmark

DISTRIBUTION OF THIS DOCUMENT IS UNLIMITED
FOREIGN SALES PROHIBITED

NT

ET-NE 98-02
ISBN 87-7475-192-1

January 1998

Basic Rotor Aerodynamics applied to Wind Turbines

Martin O.L.Hansen



Department of Energy Engineering
Fluid Mechanics

Technical University of Denmark

Printed 1998
Department of Energy Engineering
Building 404,
Technical University of Denmark
DK-2800 Lyngby

DISCLAIMER

Portions of this document may be illegible electronic image products. Images are produced from the best available original document.

Context and introduction.

The text is meant as an introduction to the basic mechanisms behind the power production of a horizontal axis wind turbine. To do so it is necessary to start with general 2-D aerodynamics in order to understand how the aerodynamic forces are produced from the flow past the blades. The text is then followed by a qualitative description of 3-D flow past a fixed wing giving rise to a vortex system in the wake changing the incoming flow. The vortex system behind a wind turbine is then extrapolated from the translating fixed wing. Then the classical 1-D analysis of Betz is introduced showing that only 59% of the available energy contained in the wind can be harvested onto a mechanical shaft. The 1-D momentum theory is then extended to the BEM method, which is used to compute the power from an actual wind turbine as a function of the wind speed. Finally, the limitations of the method and an example is shown. It should be emphasized that this material does not contain much new theory from the early work of Glauert [8], but is meant as a textbook from which one can, after a basic course in Fluid Mechanics, learn and understand some very basic rotor aerodynamics. The notes are written so that the reader can make his/her own computer program to calculate the performance of a wind turbine or a propeller. Because even though the theory is only shown for a wind turbine only slight changes must be made to compute a propeller.

3/12 - 1997 Martin O.L.Hansen

On the front page is shown the participants in la Cours course for agricultural electricians in 1904. La Cour himself is sitting as the first man from the left in the middle row. As the third man from the right in the upper row stands Johannes Juul, who introduced the modern wind turbine by connecting an asynchronous generator to a three bladed upwind stall regulated wind turbine.

2-D Aerodynamics

Two dimensional flow is comprised to a plane and if this plane is described with a coordinate system as shown in figure 1 the velocity component w in the z -direction is zero. In order to realize a 2-D flow it is necessary to extrude a profile into a wing of infinite span. On a real wing the planform, the twist and the profile changes along the span and the wing starts at a hub and ends in a tip. For long slender wings as on modern gliders and wind turbines the spanwise velocity component is normally small compared to the streamwise component and Prandtl has shown that local 2-D data can be used if the angle of attack is corrected accordingly with the trailing vortices behind the wing. These effects will be dealt with later in the section concerning 3-D aerodynamics, but it is now clear that 2-D aerodynamics is of practical interest eventhough it is difficult to realise. Figure 1 shows the leading edge stagnation point present in the 2-D flow past a profile. The reacting force F from the flow

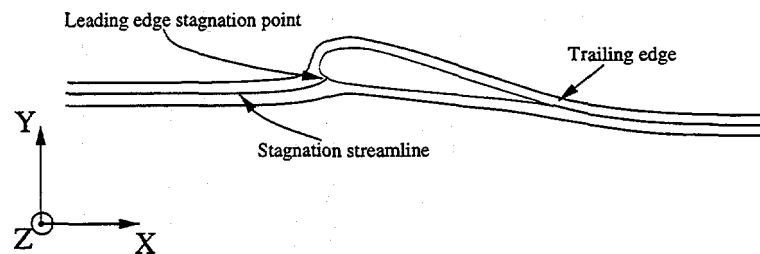


Figure 1: *Schematic view of streamlines past aerodynamic profile.*

is decomposed into a direction perpendicular to the velocity at infinity V_∞ and to a direction parallel to V_∞ . The former component is denoted the lift L and the latter is called the drag D , see figure 2. If the profile is designed for an aircraft it is obvious that the ratio L/D should be maximized. The lift is the force used to overcome gravity and the higher lift the higher mass can be lifted of the ground. In order to maintain a constant speed the drag must be balanced by a propulsion force delivered from an engine, and the smaller the drag the smaller the required engine. The lift and drag coefficients C_l and C_d are defined as

$$C_l = \frac{L}{\frac{1}{2}\rho V_\infty^2 c}, \quad (1)$$

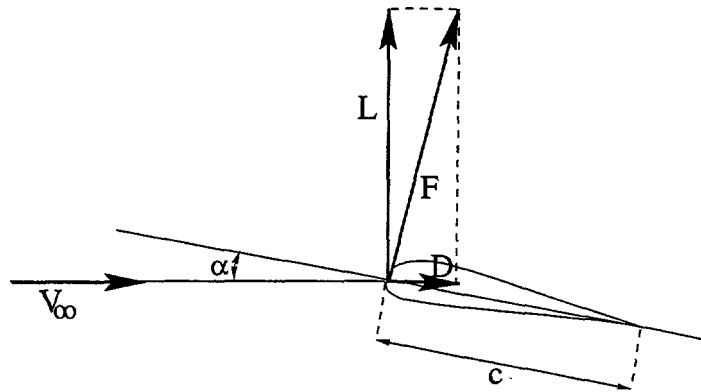


Figure 2: Definition of lift and drag.

$$C_d = \frac{D}{\frac{1}{2}\rho V_\infty^2 c}, \quad (2)$$

where ρ is the density and c the length of the profile. c is denoted the chord of the airfoil. A chordline can be defined as the line from the trailing edge to the nose of the profile, see figure 3. To describe the forces completely it is also necessary to know the moment M about a point in the profile. This point is often located on the chordline at $c/4$ from the leading edge, see figure 3. The

Typical point to measure the moment acting on the profile

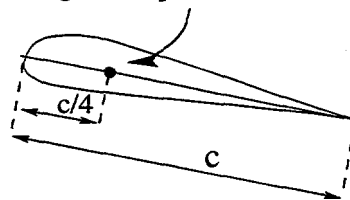


Figure 3: Typical position of the measured moment on an aerodynamic profile.

moment is positive when it tends to turn the profile on figure 3 clockwise (nose up). A moment coefficient is defined as

$$C_m = \frac{M}{\frac{1}{2}\rho V_\infty^2 c^2}, \quad (3)$$

The physical explanation of the lift is that the shape of the airfoil forces the streamlines to curve around the geometry of the profile, as indicated in figure 4. From basic fluid mechanics is known that a pressure gradient, $\frac{\partial p}{\partial r} = \rho \frac{V^2}{r}$, is necessary to curve the streamlines. r is the curvature of the streamline and V the speed. This pressure gradient acts like the centripetal force known from the circular motion of a particle. Since there is atmospheric pressure p_a far from the airfoil there must thus be a lower than atmospheric pressure on the upper side of the profile and a higher than atmospheric pressure on the lower side of the airfoil. This pressure difference gives a lifting force on the airfoil. When the airfoil is almost aligned with the flow the boundary layer stays attached and the associated drag is mainly caused by friction with the air. The coefficients C_l , C_d and C_m are functions of α , Re , Ma . α is the

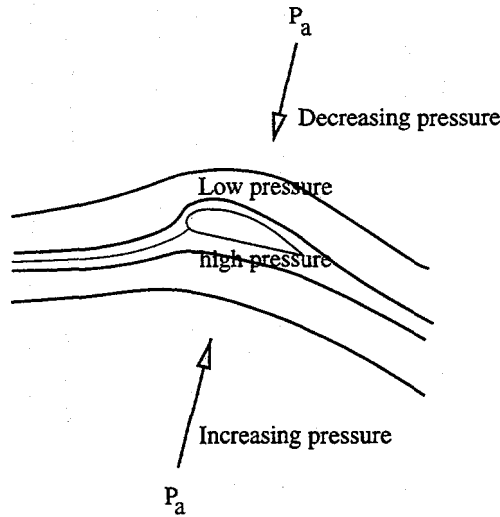


Figure 4: *Explanation of the generation of lift.*

angle of attack defined as the angle between the chordline and V_∞ , Re is the Reynolds number based on the chord and V_∞ , i.e. $Re = \frac{\rho V_\infty}{\nu}$, where ν is the kinematic viscosity. Ma denotes the Mach number, i.e. the ratio between V_∞ and the speed of sound. For a wind turbine and a slow moving aircraft the lift, drag and moment coefficients are only functions of α and Re . For a given profile the behaviour of C_l , C_d and C_m are measured and plotted in so called polars. An example of a polar for the FX67-K-170 profile is given in figure 5. C_l increases linearly with α , with an approximate slope of $2\pi/rad$, until a certain value of α , where a maximum value of C_l is reached. Hereafter the profile is said to stall and C_l decreases in a very geometry dependent manner. For small angles of attack the drag coefficient C_d is almost constant, but in-

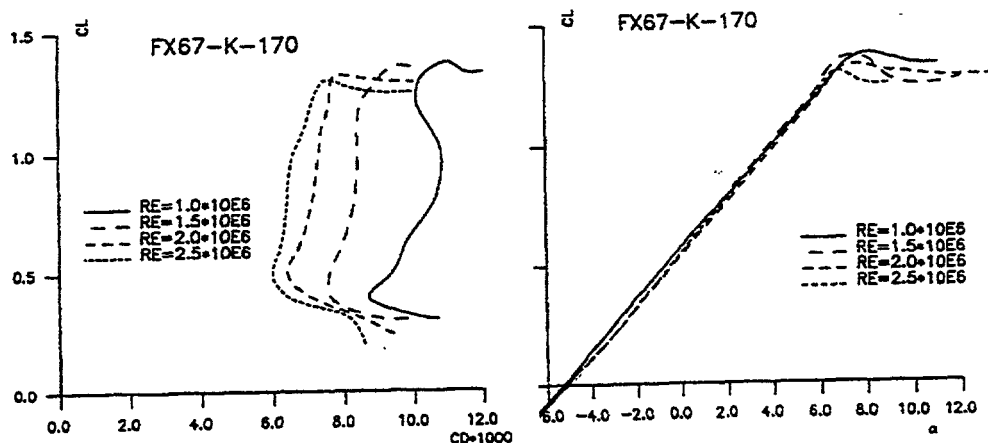


Figure 5: Polar for the FX67-K-170 profile.

creases rapidly after stall. The Reynolds number dependency can also be seen in figure 5. It is seen, especially on the drag, that as the Reynolds number reaches a certain value the Reynolds number dependency becomes small. The Reynolds number dependency is related to the point on the airfoil, where the boundary layer transition from laminar to turbulent flow occurs. The way a profile stalls is very dependent on the geometry of the profile. Thin profiles with a sharp nose, i.e. high curvature around the leading edge, tends to stall more abruptly than thick airfoils. The different stall behaviours is seen in figure 6, where $C_l(\alpha)$ is compared for two different airfoils. The FX38-153 is seen to lose its lift more rapidly than the FX67-K-170. The explanation lies in the way the boundary layer separates from the upper side of the airfoil. If the separation starts at the trailing edge of the airfoil and increases slowly with increasing angle of attack a soft stall is observed, but if the separation starts at the leading edge of the profile the entire boundary layer may separate almost simultaneously with a dramatic loss of lift. The behaviour of the viscous boundary layer is very complex and depends among other things on the curvature of the profile, the Reynolds number, surface roughness and for high speeds also on the Mach number. Some description of the viscous boundary layer will be given later in this text but for a more elaborate description it is referred to standard textbooks on viscous boundary layers as White [1] and Schlichting [2].

The forces on the profile stems from the pressure distribution $p(x)$ and the skin friction with the air $\tau_w(x) = \mu \partial u / \partial y|_{y=0}$. (x, y) is the surface coordinate system as shown in figure 7 and μ is the dynamic viscosity. The skin friction

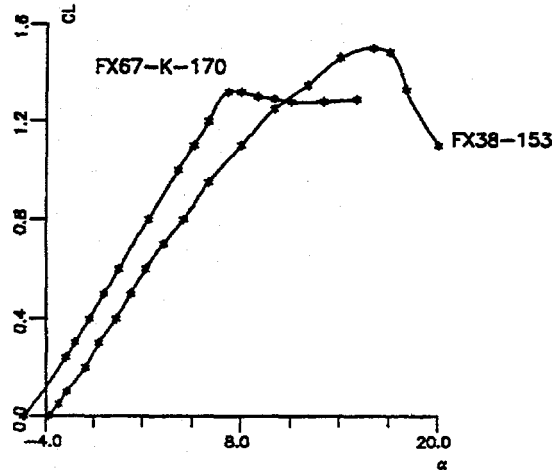


Figure 6: *Different stall behaviour.*

is mainly contributing to the drag, whereas the force found from integrating the pressure has a lift and drag component. The drag component from the pressure distribution is known as the form drag and becomes very large when the profile stalls. The stall phenomena is closely related to separation of the boundary layer, see next paragraph. Therefore rule number one in reducing drag is to avoid separation. In [3] a lot of data can be found for the NACA profiles, which have been extensively used on small aircrafts, wind turbines and helicopters.

Close to the profile there exist a viscous boundary layer due to the no-slip condition on the velocity at the wall, see figure 7. A boundary layer thickness is often defined as the normal distance $\delta(x)$ from the wall where $\frac{u(x)}{U} = 0.99$. Further, the displacement thickness $\delta^*(x)$, the momentum thickness $\theta(x)$ and the shape factor $H(x)$ are defined as

$$\delta^*(x) = \int_0^{\delta} \left(1 - \frac{u}{U}\right) dy, \quad (4)$$

$$\theta(x) = \int_0^{\delta} \frac{u}{U} \left(1 - \frac{u}{U}\right) dy, \quad (5)$$

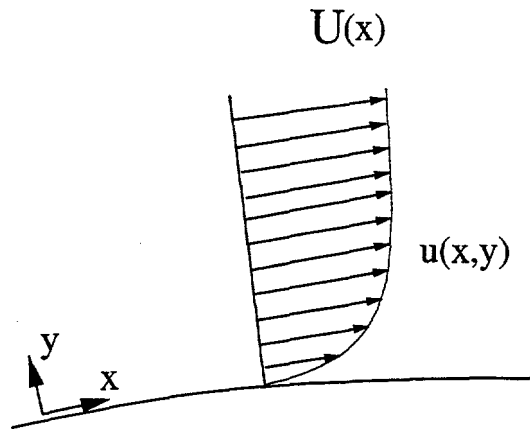


Figure 7: Viscous boundary layer at the wall of the profile.

$$H(x) = \frac{\delta^*(x)}{\theta(x)}. \quad (6)$$

The coordinate system (x, y) is a local system, where $x = 0$ is at the leading edge stagnation point and y is the normal distance from the wall. A turbulent boundary layer separates for H between 2 and 2.4. The stagnation streamline, see figure 1 divides the fluid that flow over the profile from the fluid that flow under the profile. At the stagnation point the velocity is zero and the boundary layer thickness is small. The fluid, which flow over the profile, is accelerating as it passes the leading edge and since the leading edge is close to the stagnation point and the flow is accelerating the boundary layer is thin. It is known from viscous boundary layer theory [1] that the pressure is approximately constant from the surface to the edge of the boundary layer $\partial p / \partial y = 0$. Outside the boundary layer Bernoullis equation is valid and since the flow is accelerating the pressure decreases, i.e. $\partial p / \partial x < 0$. On the lower side the pressure gradient is much smaller since the curvature of the wall is small compared to the leading edge. At the trailing edge the pressure must be the same at the upper and lower side (The Kutta condition) and therefore the pressure must rise $\partial p / \partial x > 0$ from a minimum value somewhere on the upper side to the trailing edge. An adverse pressure gradient $\partial p / \partial x > 0$ may lead to separation. This can be seen directly from the Navier-Stokes equations, which applied at the wall where the velocity is zero reduces to

$$\frac{\partial^2 u}{\partial y^2} = \frac{1}{\mu} \frac{\partial p}{\partial x}. \quad (7)$$

The curvature of the u -velocity component at the wall is therefore given by the sign of the pressure gradient. Further, it is known that $\partial u / \partial y = 0$ at $y = \delta$. From this can be deduced that the u velocity profile in an adverse pressure gradient $\partial p / \partial x > 0$ is S-shaped and separation may occur, whereas the curvature of the u -profile for $\partial p / \partial x < 0$ is negative throughout the entire boundary layer and the boundary layer stays attached. A schematic picture showing the different shapes of the boundary layer is found in figure 8. Since

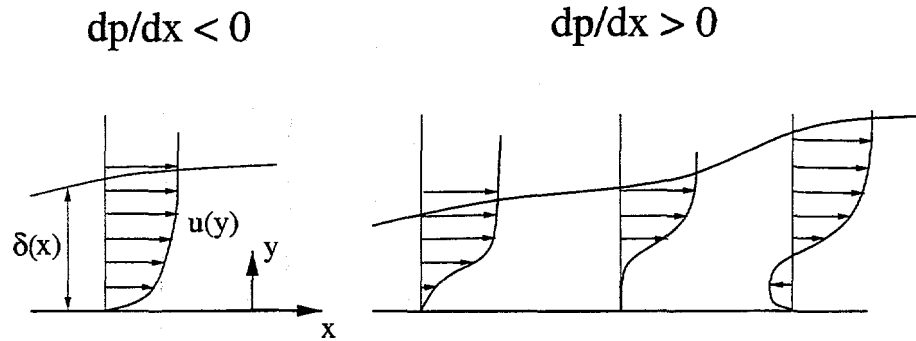


Figure 8: Schematic view of the shape of the boundary layer for a favourable and an adverse pressure gradient.

the form drag increases dramatically when the boundary layer separates, it is of utmost importance to the performance of a profile to control the pressure gradient.

For small values of x the flow is laminar, but for a certain x_{trans} the laminar boundary layer becomes unstable and a transition from laminar to turbulent flow occurs. At x_T the flow is fully turbulent. In figure 9 the transition is sketched. The transitional process is very complex and not yet fully under-

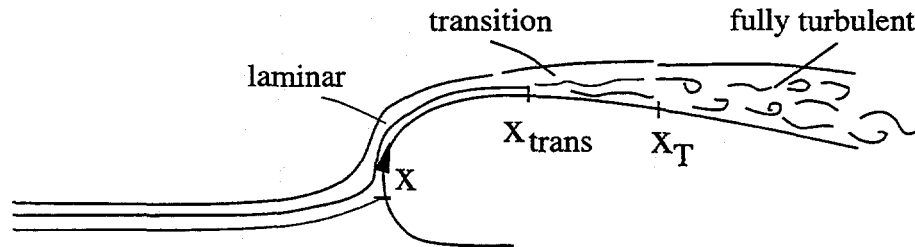


Figure 9: Schematic view of the transitional process.

stood, but a description of the phenomena is found in White [1], who also gives some engineering tools to predict x_{trans} . One of the models, which is often used in profile computations, is called the one-step method of Michel. The method predicts transition when

$$Re_\theta = 2.9 Re_x^{0.4}, \quad (8)$$

where $Re_\theta = U(x)\theta(x)/\nu$ and $Re_x = U(x)x/\nu$. For a laminar profile (see later) the method of Michel is bad and more advanced methods as the e^9 method must be applied [1].

Turbulent flow is characterized by being more stable in regions of adverse pressure gradients $\partial p/\partial x > 0$ and by a steeper velocity gradient at the wall $\partial u(x)/\partial y|_{y=0}$. The first property is good since it delays stall but the second property increases the skin friction and thus the drag. These two phenomena are exploited in the design of high performance profiles denoted laminar profiles. A laminar profile is a profile where a large fraction of the boundary layer is laminar and attached. To design such a profile it is necessary to specify the maximum angle of attack, where the boundary layer to a large extent is supposed to be laminar. The profile is then constructed so that the velocity at the edge of the boundary layer $U(x)$ is constant after the acceleration past the leading edge and downstream. It is known from boundary layer theory, [1] and [2] that the pressure gradient is expressed by the velocity outside the boundary layer as

$$\frac{dp}{dx} = -\rho U(x) \frac{dU(x)}{dx}. \quad (9)$$

At this angle the pressure gradient is therefore zero and no separation will occur. For smaller angles of attack the flow $U(x)$ will accelerate and dp/dx becomes negative, which again avoids separation and is stabilizing for the laminar boundary layer and thus delaying transition. At some point x at the upper side of the profile it is, however, necessary to decelerate the flow in order to fulfill the Kutta condition, i.e. the pressure to be unique at the trailing edge. If this deceleration is started at a position where the boundary layer is laminar the boundary layer is likely to separate. Just after the laminar/turbulent transition the boundary layer is relatively thin and the momentum close to the wall is relatively large and is therefore capable to withstand a high positive pressure gradient without separation. During the continuous deceleration

towards the trailing edge the ability of the boundary layer to withstand the positive pressure gradient is diminishing and to avoid separation it is therefore necessary to decrease the deceleration towards the trailing edge. It is of utmost importance to insure that the boundary layer is turbulent before decelerating $U(x)$ and to insure this one can trigger a turbulent transition by placing a tripwire or tape before the point of deceleration. A laminar profile is thus characterized by a high value of the lift to drag ratio C_l/C_d below the design angle. But before choosing such a profile it is important to consider the stall characteristic and the roughness sensitivity. On an airplane it is necessary to fly with a high C_l at landing since the speed is relatively small. If the pilot exceeds $C_{l,max}$ and the profile stalls it could be devastating if C_l drops as drastically with the angle of attack as on the FX38-153 in figure 6. The aeroplane will then lose its lift and might slam into the ground. If the profile is sensitive to roughness the good performance is lost if the wings are contaminated by i.e. dust, rain particles or bugs. On a wind turbine this could alter the performance with time if for instance the turbine is placed on an area with many bugs. If a wind turbine is situated near a coast salt might build up on the blades if the wind comes from the sea and if the profiles used are sensitive to roughness the power output from the turbine is dependent on the direction of the wind.

3-D Aerodynamics

This section concerning the 3-D flow past a wing will be of a qualitative nature. Some basic knowledge of this flow is, however, necessary in understanding the Blade Element Momentum method used to compute the performance of a wind turbine or a propeller. A wing is a beam of finite length with aerodynamic profiles as cross sections. There will therefore be a pressure difference between the lower and upper side of the wing, giving rise to the lift. At the tips there are leakages, where air flows around the tip from the lower side to the upper side. Therefore the streamlines flowing over the wing will be deflected inwards and the streamlines flowing under the wing will be deflected outwards. At the trailing edge there is therefore a jump in the tangential velocity, see figure 10 and figure 11. Because of this jump there is a continuous sheet of tangen-

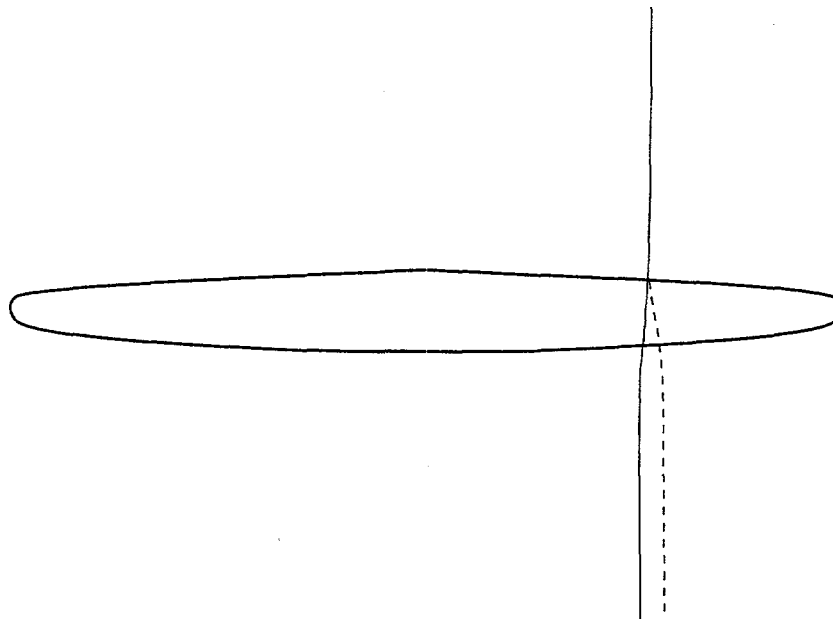


Figure 10: *Streamlines flowing over and under a wing. The wing is seen from the suction side. The streamline flowing over the suction side (full line) is deflected inwards and the streamline flowing under (dashed line) is deflected outwards.*

tial vorticity in the wake behind a wing. This sheet is denoted the free vortices.

In classic literature concerning theoretical aerodynamics like Milne-Thomson [4] it is shown that an airfoil for small angles of attack can be modelled by

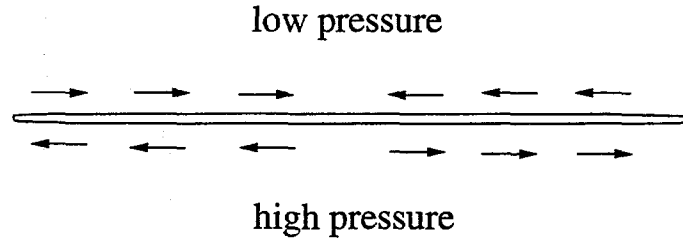


Figure 11: *Velocity vectors seen from behind a wing. A jump in the tangential velocity is seen, due to the leakage at the tips.*

a vortex filament of strength Γ . This is because the flow for small angles of attack is mainly inviscid and governed by the linear Laplace equation, and it can be shown analytically that for this case the lift is given by

$$\mathbf{L} = \rho \mathbf{V}_{\infty} \times \Gamma. \quad (10)$$

I.e. the airfoil may be substituted by a vortex filament of strength Γ . The lift produced by a 3-D wing can therefore for small angles of attack be modelled by a series of vortex filaments oriented in the spanwise direction of the wing, known as the bound vortices. According to Helmholtz theorem, see [4], a vortex filament, however, cannot terminate in the interior of the fluid but must either terminate on the boundary or be closed. A complete wing may be modelled by a series of vortex filaments Γ_i , $i=1,2,3,4,\dots$, which are oriented as shown on figure 12. The vortex filaments are strongest at the tip and decreases inboard of the wing. In a real flow the free vortices will curl up around these strong tipvortices and the vortex system will look more like figure 13. The model based on discrete vortices as shown on figure 12 is called the lifting line theory, see [5] for a complete description. The vortices on the wing (bound vortices) model the lift of the wing and the vortices in the flow direction (free vortices) model the vortex sheet stemming from the three dimensionality of the wing. The free vortices induce by the law of Biot-Savart a downwards velocity component w at any position of the wing. For one vortex filament of strength Γ the induced velocity in a point p is (see figure 14)

$$\mathbf{w} = \frac{\Gamma}{4\pi} \oint \frac{\mathbf{r} \times \mathbf{ds}}{r^3}. \quad (11)$$

The total induced velocity from all vortices at a section of the wing is known as

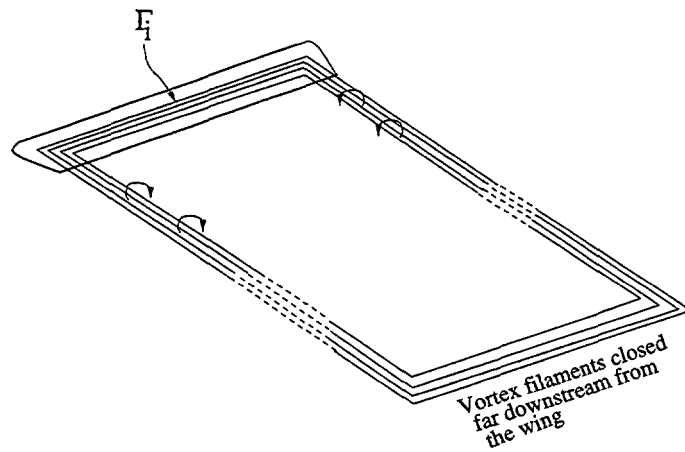


Figure 12: A simplified model of the vortical system on a wing.

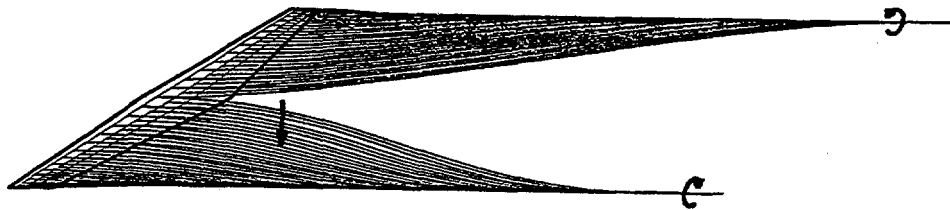


Figure 13: More realistic vortex system on a wing.

the downwash, and the local angle of attack at this section is therefore reduced by α_i , since the relative velocity is the vector sum of the wind speed V_∞ and the induced velocity w . α_g , α_i and α_e denotes the geometrical-, the induced- and the effective angle of attack, respectively. The effective angle of attack is

$$\alpha_e = \alpha_g - \alpha_i. \quad (12)$$

On figure 15 the induced velocity w , the onset flow V_∞ and the effective velocity V_e is shown for a section on the wing together with the different angles of attack α_g , α_i and α_e . From potential theory, which however is only valid for angles of attack below stall, it is known that the lift is perpendicular to the velocity seen by the profile, see equation (10). On figure 15 this force

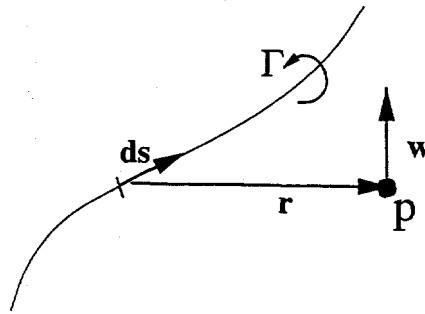


Figure 14: Induced velocity from a vortex line of strength Γ .

is denoted R . The lift is, however, by definition the force perpendicular to the onset flow V_∞ , and the resulting force is therefore decomposed into a component perpendicular to and a component in the direction of V_∞ . The former component is thus the lift and the latter is a drag denoted the induced drag D_i . At the tips of the wing the induced velocity obtains a value, which exactly gives zero lift.

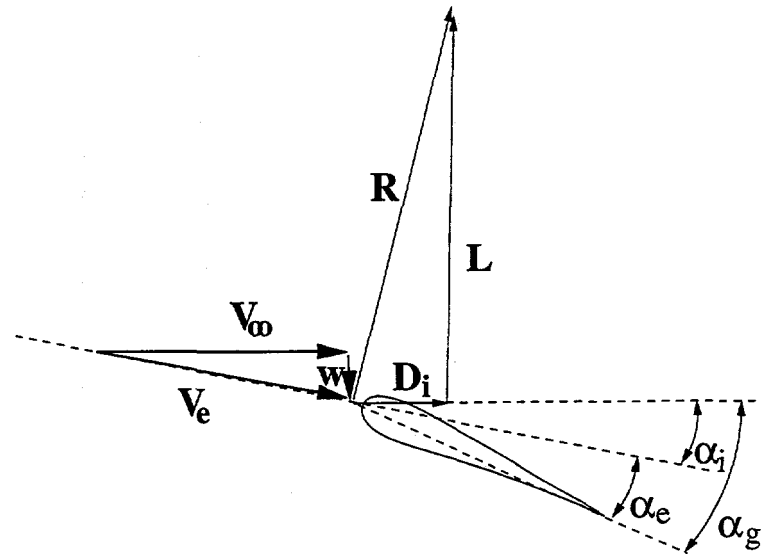


Figure 15: The effective angle of attack for a section in a wing and the resulting force R , the lift L and the induced drag D_i .

An important conclusion is thus:

For a three-dimensional wing the lift is reduced compared to a two-dimensional wing at the same geometrical angle of attack and the local lift has a component denoted the induced drag in the direction of the onset flow. Both effects are due to the velocity induced by the vortex system produced by the wing.

In the lifting line theory it is assumed that the three-dimensionality is limited to the downwash, i.e. the spanwise flow is still small compared to the streamwise velocity and 2-D data can therefore be used locally if the angle of attack is modified by the downwash. This assumption is reasonable for long slender wings like on a glider plane or a wind turbine. One method to determine the value of the vortices quantitatively and thus the induced velocities is Multhopps solution of Prandtls integral equation. This method is thoroughly described in [5] and will not be shown here, but it is important to understand that the vortical system produced by a three-dimensional wing changes the local inflow conditions seen by the wing, i.e. although the flow is locally 2-D one cannot apply the geometrical angle of attack when estimating the forces on the wing. This error was done in the early propeller theory and the discrepancy between measured and computed data was believed to be caused by wrong 2-D airfoil data. But in fact also the vortex system behind a propeller or a wind turbine changes the angle of attack seen locally on the blades.

The Vortex System of a Wind Turbine

The rotor of a horizontal axis wind turbine consists of a number of blades, which are shaped as wings. If a cut is made at a radial distance r from the rotational axis as shown on figure 16 a cascade of airfoils will be observed as shown in figure 17. The local angle of attack α is given by the pitch of the

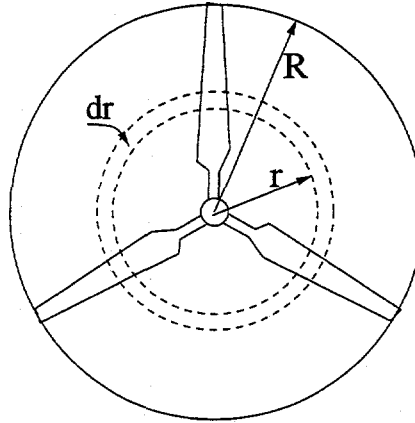


Figure 16: Rotor of a three bladed wind turbine with rotor radius R .

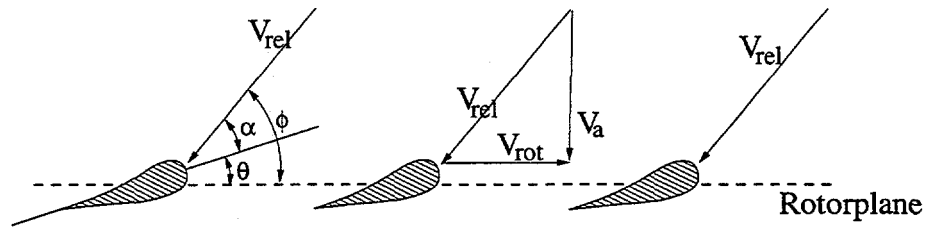


Figure 17: Aerodynamic profiles at a radial cut r/R in a wind turbine rotor.

airfoil θ , the axial velocity V_a at the rotor plane and the rotational velocity V_{rot} at the rotor plane as

$$\alpha = \phi - \theta, \quad (13)$$

where the flowangle is found as

$$\phi = \text{atan}\left(\frac{V_a}{V_{rot}}\right). \quad (14)$$

Since a horizontal axis wind turbine consists of rotating wings a vortex system similar to the linear translating wing must exist. The vortex sheet of the free vortices are oriented in a helical path behind the rotor. The strong tip vortices are located at the edge of the rotor wake and the root vortices lies mainly in a linear path along the axis of the rotor, see figure 18. The vortex

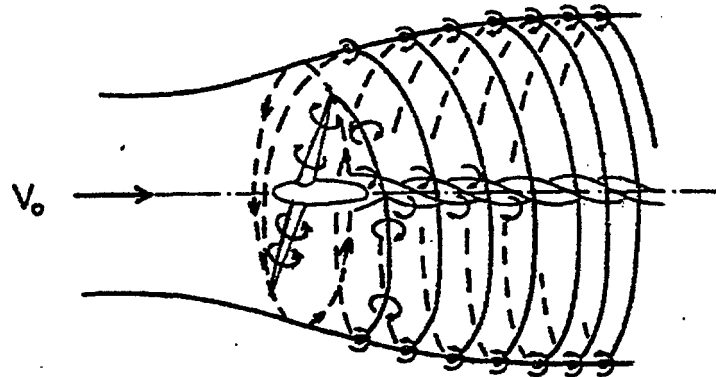


Figure 18: Schematic drawing of the vortex system behind a wind turbine. The picture is borrowed from [6].

system induces for a wind turbine a velocity, which has an axial component in the negative wind direction and a tangential component in the opposite direction of the rotation of the rotor. It is common to assume that the rotor has an infinite number of blades, since this implies that the induced velocity is constant in the azimuthal direction and is only a function of the radius. The induced velocity in the axial direction is given by the axial induction factor a as aV_0 , where V_0 is the undisturbed wind speed. The induced velocity in the tangential direction in the rotor wake is given by the tangential induction factor a' as $2a'\Omega r$ and since the flow does not rotate upstream of the rotor the tangential induced velocity in the rotor plane is approximately $a'\Omega r$. Ω denotes the angular velocity of the rotor and r is the radial distance from the

rotational axis. If a and a' are known a 2-D equivalent angle of attack could be found from equations (13) and (14), where

$$V_a = (1 - a)V_o, \quad (15)$$

and

$$V_{rot} = (1 + a')\Omega r. \quad (16)$$

If then also the lift and drag coefficients $C_l(\alpha)$ and $C_d(\alpha)$ are known for the different profiles used on the blades it is easy to compute the force distribution and further, if this distribution is integrated along the span one can compute global loads such as the power output and the root bending moments on the blades. It is the purpose of the Blade Element Momentum method to compute the induction factors a and a' and thus the loads on a wind turbine.

1-D Momentum Theory for an ideal Wind Turbine

Before deriving the Blade Element Momentum method it is useful to examine a simple 1-D model for an ideal rotor. A wind turbine extracts mechanical energy from the kinetic energy of the wind. The rotor is in this simple 1-D model a permeable disc, which slows down the axial speed V_o contained in the wind. The disc is considered ideal, i.e. it is frictionless and there is no rotational velocity component in the wake. The latter can be obtained by applying two contra rotating rotors or by using a stator. The rotor disc acts as a drag device slowing the wind speed down from V_o far upstream of the rotor to u at the rotorplane and to u_1 in the wake. Therefore the streamlines must diverge as shown in figure 19. The drag is obtained due to a pressure drop over the rotor. Close upstream of the rotor there is a small pressure rise from the atmospheric level p_o to p before a discontinuous pressure drop Δp over the rotor. Downstream of the rotor the pressure recovers continuously to the atmospheric level. Since the Mach number is small the air density is constant and the axial velocity must decrease continuously from V_o to u_1 . The behaviour of the pressure and axial velocity is shown graphically in figure 19. Due to the assumptions of an ideal rotor it is possible to derive relationships

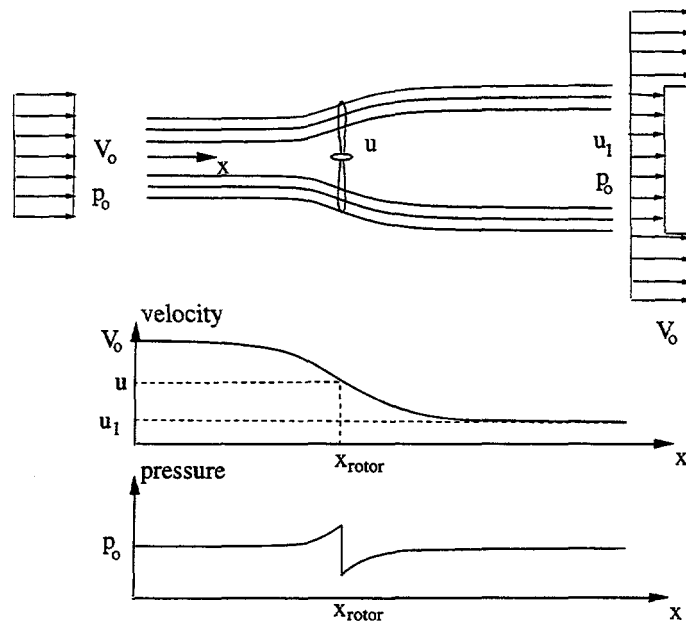


Figure 19: *Illustration of the influence of a wind turbine on the streamlines past the rotor and the axial velocity and pressure.*

between the velocities V_o , u_1 , u and the thrust T and absorbed shaft power P . The thrust is the force in the streamwise direction, which must be outbalanced by the tower

$$T = \Delta p A, \quad (17)$$

where $A = \pi R^2$ is the area of the rotor. The flow is stationary, incompressible, frictionless and no external force is acting on the fluid up- and downstream of the rotor. Therefore it is allowed to apply Bernoulli's equation from far upstream to just in front of the rotor and from just behind the rotor to far downstream in the wake.

$$p_o + \frac{1}{2}\rho V_o^2 = p + \frac{1}{2}\rho u^2 \quad (18)$$

and

$$p - \Delta p + \frac{1}{2}\rho u^2 = p_o + \frac{1}{2}\rho u_1^2. \quad (19)$$

Combining equation (18) and (19) gives

$$\Delta p = \frac{1}{2}\rho(V_o^2 - u_1^2). \quad (20)$$

The axial momentum equation on integral form is applied on the circular control volume with sectional area A_{cv} drawn with a dashed line on figure 20

$$\frac{\partial}{\partial t} \iiint_{CV} U \rho d(vol) + \iint_{CS} U \rho \mathbf{V} \cdot d\mathbf{A} = F_{ext} + F_{pres} \quad (21)$$

$d\mathbf{A}$ is a vector pointing in the normal direction of an infinitesimal part of the surface with a length equal to the area of this element. F_{pres} is the axial component of the pressure forces acting on the control volume and vol denotes an incremental part of the control volume. The first term in equation (21) is zero since the flow is assumed stationary and the last term is zero since the

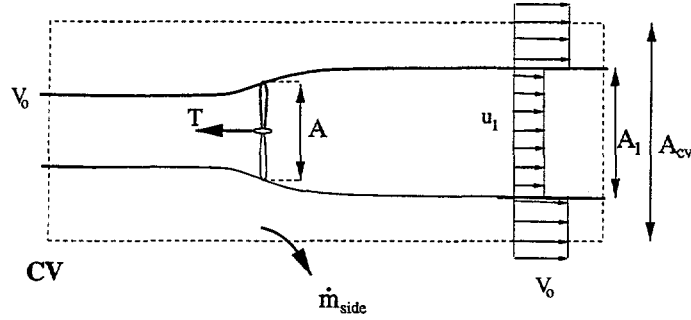


Figure 20: Circular control volume around a wind turbine.

pressure has the same atmospheric value on the end planes and acts on an equal area. Further, on the lateral boundary of the control volume the force from the pressure has no axial component. Under the simplified assumptions of an ideal rotor equation (21) then yields

$$\rho u_1^2 A_1 + \rho V_o^2 (A_{cv} - A_1) + \dot{m}_{side} V_o - \rho V_o^2 A_{cv} = -T \quad (22)$$

\dot{m}_{side} can be found from the conservation of mass

$$\rho A_1 u_1 + \rho (A_{cv} - A_1) V_o + \dot{m}_{side} = \rho A_{cv} V_o, \quad (23)$$

yielding

$$\dot{m}_{side} = \rho A_1 (V_o - u_1). \quad (24)$$

The continuity of mass also gives a relation between A and A_1 as

$$\dot{m} = \rho u A = \rho u_1 A_1. \quad (25)$$

The equations (24), (25) and (22) can be combined to

$$T = \rho u A (V_o - u_1) = \dot{m} (V_o - u_1) \quad (26)$$

If the thrust is replaced by the pressure drop over the rotor as in equation (17) and the pressure drop found in equation (20) is used an interesting observation is made.

$$u = \frac{1}{2}(V_o + u_1). \quad (27)$$

It is seen that the velocity in the rotor plane has dropped half the way to its final value u_1 in the wake.

An alternative control volume to the one in figure 20 can be made, see figure 21. The force from the pressure distribution along the lateral walls $F_{press,lateral}$

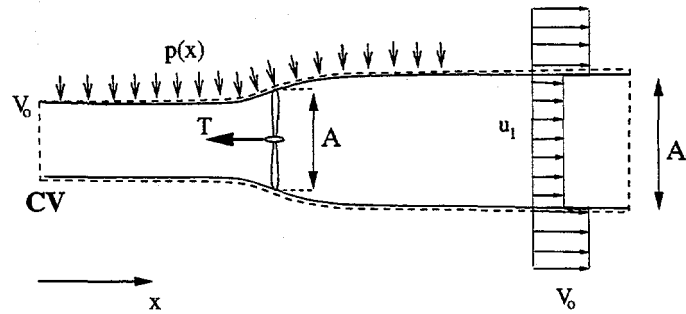


Figure 21: Alternative control volume around a wind turbine.

of the control volume is unknown and thus also the net pressure contribution F_{pres} . On this alternative control volume there is no mass flow \dot{m}_{side} through the lateral boundary, since this is aligned with the streamlines. The axial momentum equation (21) therefore becomes

$$T = \rho u A (V_o - u_1) + F_{pres}. \quad (28)$$

Since the physical problem is the same, whether the control volume in figure 20 or 21 is applied it can be seen by comparing equation (28) with (26) that the net pressure force on the control volume following the streamlines is zero.

The flow is assumed frictionless and there is therefore no changes in the internal energy from the inlet to the outlet and the shaft power P can be found

using the integral energy equation on the control volume shown in figure 21

$$P = \dot{m} \left(\frac{1}{2} V_o^2 + p_o / \rho - \frac{1}{2} u_1^2 - p_o / \rho \right) \quad (29)$$

and since $\dot{m} = \rho u A$ the equation for P becomes

$$P = \frac{1}{2} \rho u A (V_o^2 - u_1^2). \quad (30)$$

The axial induction factor a is introduced as

$$u = (1 - a) V_o. \quad (31)$$

Combining equation (31) with (27) gives

$$u_1 = (1 - 2a) V_o, \quad (32)$$

which can be introduced in equation (30) for the power P and in equation (26) for the thrust T , yielding

$$P = 2 \rho V_o^3 a (1 - a)^2 A \quad (33)$$

and

$$T = 2 a \rho V_o^2 (1 - a) A. \quad (34)$$

The available power in a cross section equal to the swept area A by the rotor is

$$P_{avail} = \frac{1}{2} \dot{m} V_o^2 = \frac{1}{2} \rho V_o^3 A. \quad (35)$$

The power P is often non-dimensionalized with respect to P_{avail} in a power coefficient C_p

$$C_p = \frac{P}{\frac{1}{2}\rho V_o^3 A}. \quad (36)$$

Similar a thrust coefficient C_T is defined as

$$C_T = \frac{T}{\frac{1}{2}\rho V_o^2 A}. \quad (37)$$

Using equations (33) and (34) the power and thrust coefficient may for the ideal 1-D wind turbine be written as

$$C_p = 4a(1 - a)^2 \quad (38)$$

and

$$C_T = 4a(1 - a). \quad (39)$$

Differentiating C_p with respect to a yields

$$\frac{dC_p}{da} = 4(1 - a)(1 - 3a). \quad (40)$$

It is easy seen that $C_{p,max} = \frac{16}{27}$ for $a = \frac{1}{3}$. The equations (38) and (39) are shown graphically in figure 22.

Thus it has been shown that a theoretical maximum of $C_p = \frac{16}{27}$ exist for $a = \frac{1}{3}$ for an ideal horizontal axis wind turbine. This limit is known as the Betz limit.

Experiments have shown that the assumptions of an ideal wind turbine leading to the equations (38) and (39) are only valid for an axial induction

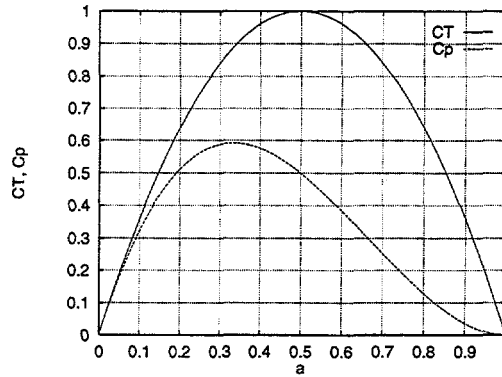


Figure 22: The power and thrust coefficients C_p and C_T as a function of the axial induction factor a for an ideal horizontal axis wind turbine.

factor of less than approximately 0.4. This is seen in figure 23 showing C_T as a function of a together with the different rotor states. If the momentum theory were valid for higher values of a the velocity in the wake would become negative as can readily be seen by equation (32). As C_T increases the expansion of the wake increases and thus the velocity jump from V_o to u_1 in the wake, see figure 24. The ratio between the areas A_o and A_1 in the figure 24 can be found directly from the continuity equation as

$$\frac{A_o}{A_1} = 1 - 2a. \quad (41)$$

A high thrust coefficient C_T and thus a high axial induction factor a is for a wind turbine present at low wind speeds. The reason that the simple momentum theory is not valid for a greater than approximately 0.4 is that the free shear layer at the edge of the wake becomes unstable when the velocity jump $V_o - u_1$ becomes too high and eddies are formed, which transport momentum from the outer flow into the wake. This situation is called the turbulent wake state, see figure 23 and 25.

Effects of rotation

One of the assumptions of the ideal rotor was that the rotation in the wake has been avoided, i.e. a' is zero. Since a modern wind turbine consist of a single rotor without a stator the wake will posses some rotation as can be seen directly from the Euler turbine equation applied on an infinitesimal control

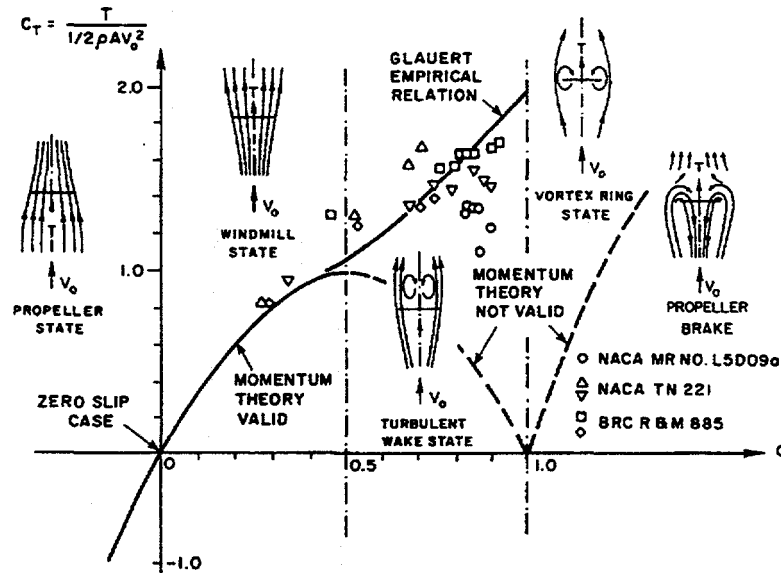


Figure 23: The measured thrust coefficient C_T as a function of the axial induction factor a and the corresponding rotor states. The figure is borrowed from [7].

volume of thickness dr as shown in figure 16

$$dP = \dot{m} \Omega r C_\theta = 2\pi r^2 \rho \Omega u C_\theta dr, \quad (42)$$

where C_θ is the azimuthal component of the absolute velocity C after the rotor and u the axial velocity through the rotor, see figure 26. From equation (42) it is seen that for a given power P and windspeed the rotational velocity component in the wake C_θ decreases with increasing rotational speed Ω of the rotor. From an efficiency point of view it is therefore desirable to have a high rotational speed of the wind turbine to minimize the loss of kinetic energy contained in the rotating wake. If we recall that the axial velocity through the rotor is given by the axial induction factor a as equation (31) and that the rotational speed in the wake is given by a' as

$$C_\theta = 2a'\Omega r, \quad (43)$$

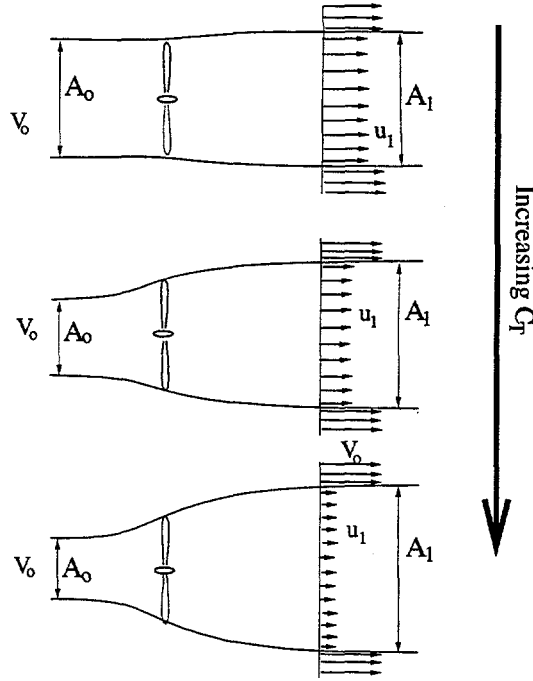


Figure 24: The expansion of the wake and the velocity jump in the wake for the 1-D model of an ideal wind turbine.

equation (42) may be written

$$dP = 4\pi\rho\Omega^2 V_0 a'(1-a)r^3 dr. \quad (44)$$

The total power is found by integrating dP from 0 to R as

$$P = 4\pi\rho\Omega^2 V_0 \int_0^R a'(1-a)r^3 dr \quad (45)$$

or in non-dimensional form as

$$C_p = \frac{8}{\lambda^2} \int_0^\lambda a'(1-a)x^3 dx, \quad (46)$$

where $\lambda = \frac{\Omega R}{V_0}$ is the tip speed ratio and $x = \frac{\Omega r}{V_0}$ is the local rotational speed at the radius r non-dimensionalized with respect to the wind speed V_0 . It is

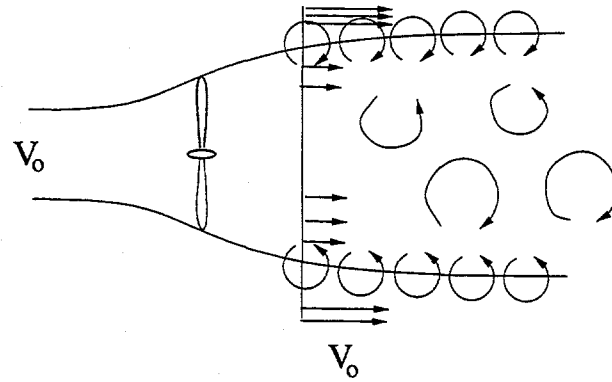


Figure 25: Schematic view of the turbulent wake state induced by the unstable shear flow at the edge of the wake.

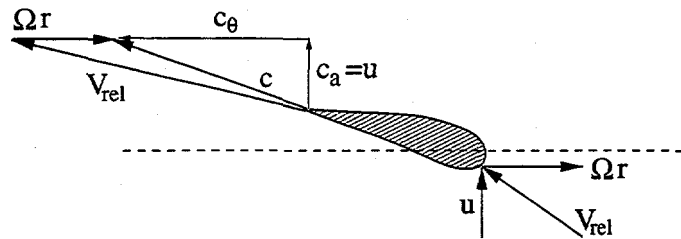


Figure 26: The velocity triangle for a section of the rotor.

clear from equations (45) and (46) that in order to optimize the power it is necessary to maximize the expression

$$f(a, a') = a'(1 - a). \quad (47)$$

If the local angles of attack are below stall a and a' are not independent since the reacting force according to potential flow theory is perpendicular to the local velocity seen by the blade and given by equation (10). The total induced velocity w must be in the same direction as the force and thus also be perpendicular to the local velocity. Employing this one can derive from figure 27 that

$$x^2 a'(1 + a') = a(1 - a), \quad (48)$$

since

$$\tan\phi = \frac{a'\Omega r}{aV_o} \quad (49)$$

and

$$\tan\phi = \frac{(1-a)V_o}{(1+a')\Omega r}. \quad (50)$$

$x = \frac{\Omega r}{V_o}$ denotes the local rotational speed to the wind speed. For local angles

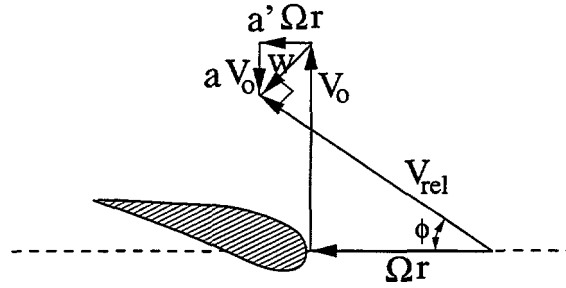


Figure 27: Velocity triangle showing the induced velocities for a section of the blade. Note that for small angles of attack the total induced velocity w is perpendicular to the relative velocity seen by the section

of attack below stall a and a' are related through equation (48) and the optimization problem is thus to maximize (47) and still satisfying equation (48). If a' is a function of a the expression (47) is maximal when $\frac{df}{da} = 0$ yielding

$$\frac{df}{da} = (1-a)\frac{da'}{da} - a' = 0 \quad (51)$$

\Downarrow

$$(1-a)\frac{da'}{da} = a'. \quad (52)$$

Equation (48) is differentiated with respect to a

$$(1 + 2a') \frac{da'}{da} x^2 = 1 - 2a. \quad (53)$$

If equation (52) and (53) is combined with equation (48) the optimum relationship between a and a' can be derived

$$a' = \frac{1 - 3a}{4a - 1}. \quad (54)$$

A table between a , a' and x can now be computed. a' is given by equation (54) for a specified a and then x is found using (48).

a	a'	x
0.26	5.5	0.073
0.27	2.375	0.157
0.28	1.333	0.255
0.29	0.812	0.374
0.30	0.500	0.529
0.31	0.292	0.753
0.32	0.143	1.15
0.33	0.031	2.63
0.333	0.00301	8.58

It is seen that as the rotational speed Ω and thus $x = \frac{\Omega r}{V_\infty}$ is increased the optimum value for a tends to $\frac{1}{3}$, which was showed previously using simple momentum theory to be the optimum value for an ideal rotor. If the values from the table is used the optimum power coefficient C_p can be found by integrating equation (46). This is done in Glauert [8] for different tip speed ratios $\lambda = \frac{\Omega R}{V_\infty}$. Glauert compares this computed optimal power coefficient with the Betz limit of $\frac{16}{27}$, which is derived for zero rotation in the wake $a' = 0$.

$\lambda = \frac{\Omega R}{V_o}$	$27C_p/16$
0.5	0.486
1.0	0.703
1.5	0.811
2.0	0.865
2.5	0.899
5.0	0.963
7.5	0.983
10.0	0.987

In figure 28 the table is shown graphically and it is observed that the loss due to rotation is small for tip speed ratios greater than approximately 6.

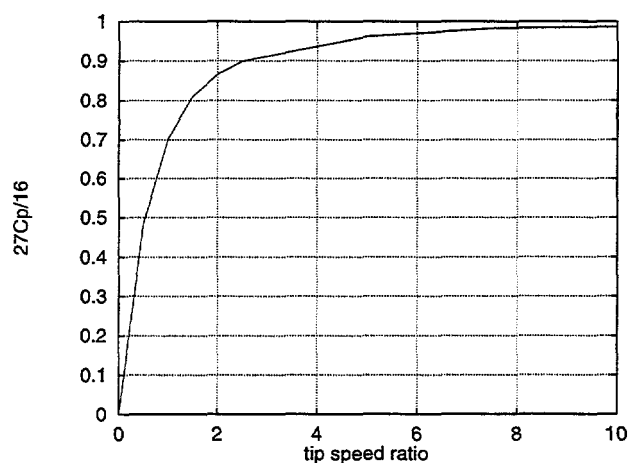


Figure 28: The efficiency of an optimal turbine with rotation. The efficiency is defined as the ratio between C_p and the Betz limit $\frac{16}{27}$.

The Blade Element Momentum method

All definitions and necessary theory have now been introduced to understand the Blade Element Momentum method BEM. Here the classical BEM model from Glauert [8] will be shown. If one, however, assumes as in the inviscid lifting line theory that only the lift is responsible for the induced velocity it is not necessary to apply both the linear momentum equation in the streamwise direction and the moment of momentum equation tangentially (see later) to derive the BEM model but it is sufficient to use the linear momentum equation in the direction of the lift, which is assumed to be perpendicular to the relative velocity seen by the rotor. The latter method is used by Øye [9] and a small difference in the computed results may be observed for high wind speeds where parts of the blades stall and viscous effects play a role. The advantage of the Øye model is fewer equations to solve and thus a faster convergence and the disadvantage is that the model might produce wrong results for high wind speeds. It has been chosen in these notes to show the classical BEM model as described in [8]. In the 1-D momentum theory the actual geometry of the rotor is not considered, i.e. the number of blades, the pitch and chord distribution and the aerodynamic profiles used. The Blade Element Momentum method couples the momentum theory with the local events taking place at the actual blades. The streamtube introduced in the 1-D momentum theory is discretized by N annular elements of height dr as shown in figure 29. The lateral boundary of these elements are streamlines, i.e. there is no flow across the elements. In the BEM model it is assumed for these annular elements

- 1) No radial dependency, i.e. what happens at one element cannot be felt by the others.
- 2) The forces from the blades on the flow is constant in each annular element. This corresponds to a rotor with an infinite number of blades.

A correction denoted Prandtl's tip loss factor is later introduced to correct for the latter assumption in order to compute a rotor with a finite number of blades.

In the previous section concerning the 1-D momentum theory it was proven that the pressure distribution along the curved streamlines enclosing the wake does not give an axial force component. Therefore it is assumed that this is also the case for the annular control volume shown in figure 29. The thrust

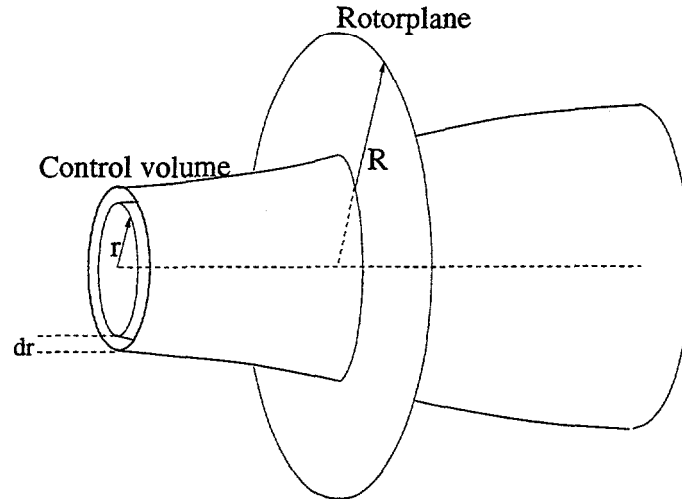


Figure 29: Control volume shaped as an annular element to be used in the BEM model.

from the disc on this control volume can thus be found from the integral momentum equation since the cross section of the control volume at the rotor plane is $2\pi r dr$

$$dT = \dot{m}(V_o - u_1) = 2\pi r \rho u (V_o - u_1) dr. \quad (55)$$

The torque dQ on the annular element is found using the integral moment of momentum equation on the control volume and applying that the rotational velocity upstream of the rotor is zero and C_θ in the wake

$$dQ = \dot{m} r C_\theta = 2\pi r^2 \rho u C_\theta dr. \quad (56)$$

This could also have been derived directly from Euler's turbine equation (42), since

$$dP = \Omega dQ. \quad (57)$$

From the ideal rotor it was found that the axial velocity in the wake u_1 could be expressed by the axial induction factor a and the wind speed V_o as $u_1 =$

$(1 - 2a)V_o$. This expression is also valid with a good approximation for a rotor with swirl in the wake. If this expression is introduced to the equations (56) and (55) together with the definitions for a and a' equations (31) and (43) the thrust and torque can be computed as

$$dT = 4\pi r \rho V_o^2 a(1 - a)dr \quad (58)$$

and

$$dQ = 4\pi r^3 \rho V_o \Omega (1 - a)a'dr. \quad (59)$$

The forces on the left hand sides of equation (58) and (59) is found from the local flow around the blade. It is recalled that the relative velocity V_{rel} seen by a section of the blade is a combination of the axial velocity $(1 - a)V_o$ and the tangential velocity $(1 + a')\Omega r$ at the rotorplane, see figure 30. θ is the

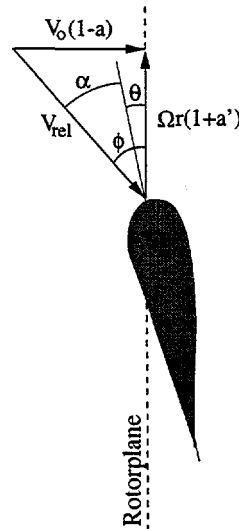


Figure 30: *Velocities at the rotorplane.*

local pitch of the blade, i.e. the local angle between the chord and the plane of rotation. ϕ is the angle between the plane of rotation and the relative velocity V_{rel} and it is seen on figure 30 that the local angle of attack is given by

$$\alpha = \phi - \theta. \quad (60)$$

Further, it is seen that

$$\tan\phi = \frac{(1-a)V_o}{(1+a')\Omega r}. \quad (61)$$

It is recalled from the section concerning 2-D aerodynamics that the lift by definition is perpendicular to the velocity seen by the profile and the drag parallel with the same velocity. In the case of a rotor this velocity is V_{rel} due to arguments given in the section about the vortex system of a wind turbine. Further, if the lift and drag coefficients C_l and C_d are known the lift L and drag D per length can be found from the equations (1) and (2)

$$L = \frac{1}{2}\rho V_{rel}^2 c C_l \quad (62)$$

and

$$D = \frac{1}{2}\rho V_{rel}^2 c C_d. \quad (63)$$

Since we are interested only in the force normal to and tangential to the rotorplane the lift and drag are projected into these directions, see figure 31

$$F_N = L\cos\phi + D\sin\phi \quad (64)$$

and

$$F_T = L\sin\phi - D\cos\phi. \quad (65)$$

The equations (64) and (65) are normalized with respect to $\frac{1}{2}\rho V_{rel}^2 c$ yielding

$$C_N = C_l\cos\phi + C_d\sin\phi \quad (66)$$

and

$$C_T = C_l\sin\phi - C_d\cos\phi, \quad (67)$$

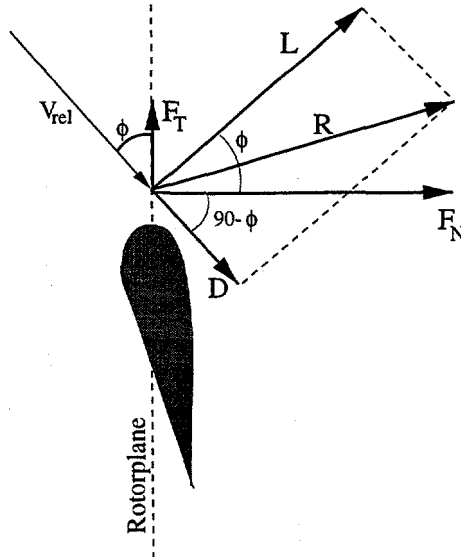


Figure 31: Figure showing the local forces on a blade. The total force R is the vector sum of the lift L and the drag D . F_N and F_T are the normal and tangential components of R , respectively.

where

$$C_N = \frac{F_N}{\frac{1}{2}\rho V_{rel}^2 c} \quad (68)$$

and

$$C_T = \frac{F_T}{\frac{1}{2}\rho V_{rel}^2 c}. \quad (69)$$

From figure 30 it is readily seen from the geometry that

$$V_{rel} \sin \phi = V_o(1 - a) \quad (70)$$

and

$$V_{rel} \cos \phi = \Omega r(1 + a'). \quad (71)$$

Further, a solidity σ is defined as the fraction of the annular area in the control volume, which is covered by the blades

$$\sigma(r) = \frac{c(r)B}{2\pi r}. \quad (72)$$

B denotes the number of blades, $c(r)$ is the local chord and r is the radial position of the control volume.

The normal force and the torque on the control volume of thickness dr is since F_N and F_T are forces per length

$$dT = BF_N dr \quad (73)$$

and

$$dQ = rBF_T dr. \quad (74)$$

Using equation (68) for F_N and equation (70) for V_{rel} equation (73) becomes

$$dT = \frac{1}{2}\rho B \frac{V_o^2(1-a)^2}{\sin^2\phi} cC_N dr. \quad (75)$$

Similarly equation (74) becomes if (69) is used for F_T and equations (70) and (71) for V_{rel}

$$dQ = \frac{1}{2}\rho B \frac{V_o(1-a)\Omega r(1+a')}{\sin\phi\cos\phi} cC_T r dr. \quad (76)$$

If the two equations (75) and (58) for dT is equalized and the definition of the solidity equation (72) is applied an expression for the axial induction factor a is obtained

$$a = \frac{1}{\left(\frac{4\sin^2\phi}{\sigma C_N} + 1\right)}. \quad (77)$$

If equations (76) and (59) are equalized an equation for a' is derived

$$a' = \frac{1}{\left(\frac{4\sin\phi\cos\phi}{\sigma C_T} - 1\right)}. \quad (78)$$

Now all necessary equations for the BEM model have been derived and the algorithm can be summarized as the 8 steps below. Since the different control volumes are assumed to be independent, each strip can be treated separately and the solution at one radius can be computed before solving for another radius, i.e. for each control volume following algorithm is applied.

- Step (1) Initialize a and a' , typically $a = a' = 0$.
- Step (2) The flowangle ϕ is computed using equation (61).
- Step (3) Compute the local angle of attack $\alpha = \phi - \theta$
- Step (4) Read $C_l(\alpha)$ and $C_d(\alpha)$ from table.
- Step (5) Compute C_N and C_T from equations (66) and (67).
- Step (6) Calculate a and a' from equations (77) and (78).
- Step (7) If a and a' has changed more than a certain tolerance
goto step (2) else finished.
- Step (8) Compute the local forces on the segment of the blades.

This is in principle the BEM method, but in order to get good results it is necessary to apply two corrections to the algorithm. The first is called Prandtl's tip loss factor, which corrects the assumption of an infinite number of blades. The second correction is called the Glauert correction and is an empirical relation between the thrust coefficient C_T and the axial interference factor a for a greater than approximately 0.3, where the relation derived from the one-dimensional momentum theory is no longer valid. Each of these corrections will be treated in separate sections.

After having applied this BEM algorithm to all control volumes the tangential and normal force distribution is known and global parameters such as the mechanical power, thrust and root bending moment can be computed. One

has, however, to be careful when integrating the tangential forces to give the shaft torque. The tangential force per length $F_{T,i}$ is known for each segment at radius r_i and a linear variation between r_i and r_{i+1} is assumed, see figure 32. The force F_T between r_i and r_{i+1} is thus

$$F_T = A_i r + B_i \quad (79)$$

where

$$A_i = \frac{F_{T,i+1} - F_{T,i}}{r_{i+1} - r_i} \quad (80)$$

and

$$B_i = \frac{F_{T,i} r_{i+1} - F_{T,i+1} r_i}{r_{i+1} - r_i} \quad (81)$$

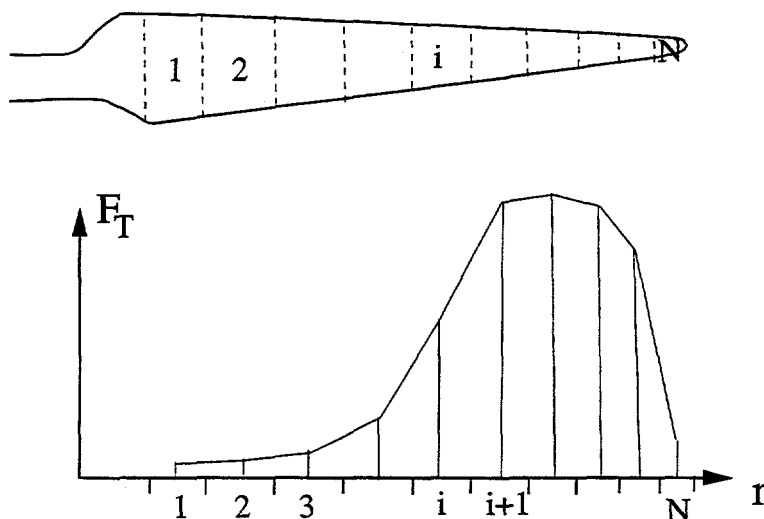


Figure 32: A linear variation of the tangential force is assumed between two different radial positions r_i and r_{i+1} .

The torque dM for an infinitesimal part of the blade of length dr is

$$dM = r F_T dr = (A_i r^2 + B_i r) dr \quad (82)$$

and the contribution $M_{i,i+1}$ to the total shaft torque from the linear tangential force variation between r_i and r_{i+1} is thus

$$M_{i,i+1} = \left[\frac{1}{3} A_i r^3 + \frac{1}{2} B_i r^2 \right]_{r_i}^{r_{i+1}}. \quad (83)$$

The total shaft torque is the sum of all the contributions $M_{i,i+1}$ along the blade

$$M_{tot} = \sum_1^{N-1} M_{i,i+1} \quad (84)$$

Prandtl's tip loss factor

As already mentioned Prandtl's tip loss factor corrects the assumption of an infinite number of blades. As has been shown previously the vortex system in the wake is different for a rotor with a finite number of blades from a rotor with an infinite number of blades. Prandtl derived a correction factor F to equations (58) and (59)

$$dT = 4\pi r \rho V_o^2 a(1-a) F dr \quad (85)$$

and

$$dQ = 4\pi r^3 \rho V_o \Omega (1-a) a' F dr. \quad (86)$$

F is computed as

$$F = \frac{2}{\pi} \arccos(e^{-f}) \quad (87)$$

where

$$f = \frac{B}{2} \frac{R-r}{r \sin \phi}. \quad (88)$$

B is the number of blades, R is the total radius of the rotor, r is the local radius and ϕ is the flowangle. Using equations (85) and (86) instead of equations (58) and (59) in deriving the equations for a and a' yields

$$a = \frac{1}{\left(\frac{4F \sin^2 \phi}{\sigma C_N} + 1\right)} \quad (89)$$

and

$$a' = \frac{1}{\left(\frac{4F \sin \phi \cos \phi}{\sigma C_T} - 1\right)}. \quad (90)$$

Equations (89) and (90) should be used instead of equations (77) and (78) in step 6 in the BEM algorithm and an extra step computing Prandtl's tip loss factor F should be put in after step 2. Deriving Prandtl's tip loss factor is very complicated and is not shown here, but a complete description can be found in [8].

Glauert correction for high values of a

When the axial interference factor becomes larger than approximately 0.3 the simple momentum theory breaks down, see figure 23. In figure 23 the different states of the rotor is also shown. Different empirical relations between C_T can be made to fit with measurements

$$C_T = \begin{cases} 4a(1-a)F & a \leq \frac{1}{3} \\ 4a(1 - \frac{1}{4}(5-3a)a)F & a > \frac{1}{3} \end{cases} \quad (91)$$

or

$$C_T = \begin{cases} 4a(1-a)F & a \leq a_c \\ 4(a_c^2 + (1-2a_c)a)F & a > a_c \end{cases} \quad (92)$$

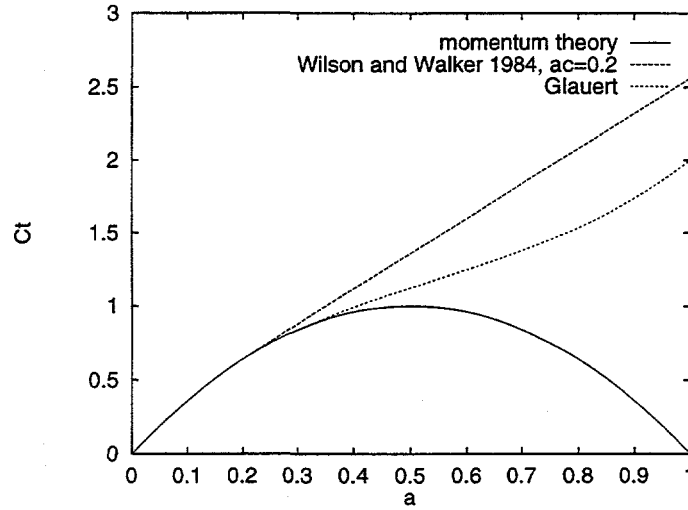


Figure 33: *Different expressions for C_T versus a .*

The last expression is found in [10] and a_c is approximately 0.2. F is Prandtl's tip loss factor and corrects the assumption of an infinite number of blades. In figure 33 the two expressions $C_T(a)$ is plotted for $F=1$ and compared to the simple momentum theory. From the local aerodynamics the thrust dT on an annular element is given by equation (75). C_T for an annular control volume is

$$C_T = \frac{dT}{\frac{1}{2}\rho V_o^2 2\pi r dr}, \quad (93)$$

Using equation (75) for dT C_T becomes

$$C_T = \frac{(1-a)^2 \sigma C_N}{\sin^2 \phi} \quad (94)$$

This expression for C_T is now equated with the empirical expression (92).

$$\underline{a \leq a_c}$$

$$4a(1-a)F = \frac{(1-a)^2 \sigma C_N}{\sin^2 \phi} \quad (95)$$

↓

$$a = \frac{1}{\frac{4F \sin^2 \phi}{\sigma C_N} + 1}, \quad (96)$$

which is the normal equation (89).

$$\underline{a > a_c}$$

$$4F(a_c^2 + (1 - 2a_c)a) = \frac{(1 - a)^2 \sigma C_N}{\sin^2 \phi} \quad (97)$$

↓

$$a = \frac{1}{2} [2 + K(1 - 2a_c) - \sqrt{(K(1 - 2a_c) + 2)^2 + 4(Ka_c^2 - 1)}], \quad (98)$$

where

$$K = \frac{4F \sin^2 \phi}{\sigma C_N} \quad (99)$$

In order to compute the induced velocities correctly for small wind speeds equation (98) and (96) must replace equation (89) from the simple momentum theory.

Annual Energy Production

The BEM method has now been derived and it is possible to compute a power curve, i.e. the shaft power as a function of the wind speed. In order to compute the annual energy production it is necessary to combine this production curve with a distribution function for the wind speed. The energy production is found by multiplying the power curve with the wind distribution curve, integrating over the velocity spectrum and finally multiplying with the number of hours per year. In practice the wind speed is discretized into N discrete values, typically with 1m/s difference (see figure 34) and the production is computed as

$$E = \sum_{i=1}^N P(V_i) \cdot h(V_i) \cdot 8700. \quad (100)$$

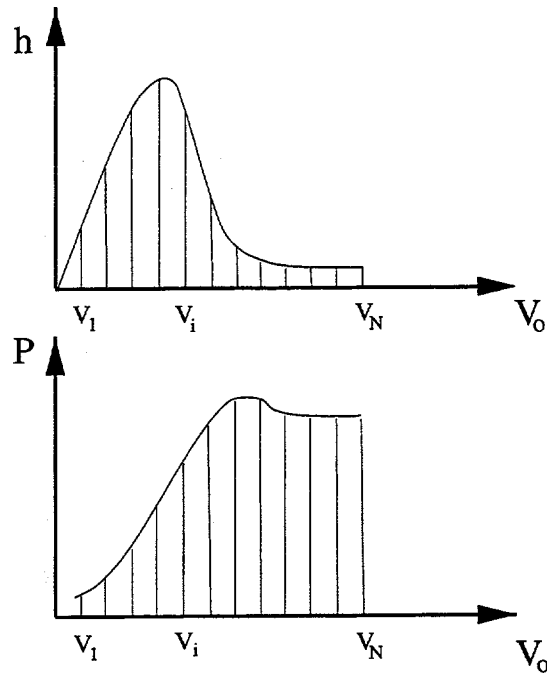


Figure 34: Distribution function for the wind speed and a power curve to compute the annual energy production for a specific turbine at a specific place.

It must be noted that the result from equation (100) must be corrected for loss in the generator and gearbox, which have a combined efficiency of approximately 0.9. Typically the wind distribution is given by either a Rayleigh or

Weibull distribution. The Rayleigh distribution is given by the mean velocity \bar{V} only as

$$h_R = \frac{\pi}{2} \frac{V_o}{\bar{V}} \exp\left(-\frac{\pi}{4} \left(\frac{V_o}{\bar{V}}\right)^2\right). \quad (101)$$

In the more general Weibull distribution some corrections for the local siting (landscape, vegetation, nearby houses, obstacles etc.) can be modelled through a scaling factor A and a form factor k

$$h_W = \frac{k}{A} \left(\frac{V}{A}\right)^{k-1} \exp\left(-\left(\frac{V}{A}\right)^k\right). \quad (102)$$

The parameters k and A must be determined from local meteorological data, nearby obstacles and landscape. A help in doing this is the 'European Wind Atlas' [11]. For a typical danish agricultural landscape the parameters are approximately $k=1.9$ and $A=6.8$.

Example

After having derived the BEM method and shown how the annual energy production can be calculated it is time for an example showing what results to expect on a real turbine. Following example is a Nordtank NKT 500/41 wind turbine. The turbine is stall regulated and the main parameters are listed below.

Fixed pitch

Rotational speed of 27.1RPM

Air density 1.225kg/m^3

Rotor radius 20.5m

Number of blades 3

Hub height 35.0m

Cut in wind speed 4m/s and cut out wind speed 25m/s

Description of blade

r [m]	twist	chord [m]
4.5	20.00	1.630
5.5	16.30	1.597
6.5	13.00	1.540
7.5	10.05	1.481
8.5	7.45	1.420
9.5	5.85	1.356
10.5	4.85	1.294
11.5	4.00	1.229
12.5	3.15	1.163
13.5	2.60	1.095
14.5	2.02	1.026
15.5	1.36	0.955
16.5	0.77	0.881
17.5	0.33	0.806
18.5	0.14	0.705
19.5	0.05	0.545
20.3	0.02	0.265

Since the power depends directly on the air density ρ the computations must according to the standards [12] be performed for $\rho = 1.225\text{kg/m}^3$. The difficult part is to find reliable data for $C_l(\alpha)$ and $C_d(\alpha)$ for the different profiles used along the span. The data available in the literature are for thin airfoils not

much thicker than 20% and for angles of attack only slightly above $C_{l,max}$. For structural reasons it is desirable to use very thick airfoils of approximately 40% of the chord at the root of the blades to absorb the high bending moments. Further, the flow past the rotating blades are influenced by centrifugal and Coriolis forces, which alter the post stall lift and drag coefficients from what can be measured in a windtunnel. It is therefore clear that it requires significant engineering skill and experience to construct airfoil data for thick airfoils at high angles of attack including 3-D effects. When the power curve from an actual wind turbine is known it is common to calibrate the airfoil data afterwards, in order to have a better agreement between measurements and computations. If a new blade is constructed, which are not too different from blades where the airfoil data has been calibrated, it is possible to predict very well the power curve. But if a new blade is to be designed with completely new airfoils one has to be very careful in using the computed results. The actual profiles and airfoil data on the blade of the Nordtank NKT 500/41 is not given here, but an experienced guess has been applied to extrapolate the data into high angles of attack. Since the power curve has been measured at Risø [13] a comparison between the computed and measured power curve is shown in figure 35 in order to get an idea of the accuracy of the BEM model. It is seen in figure 35 that except for the very low and high wind speeds the

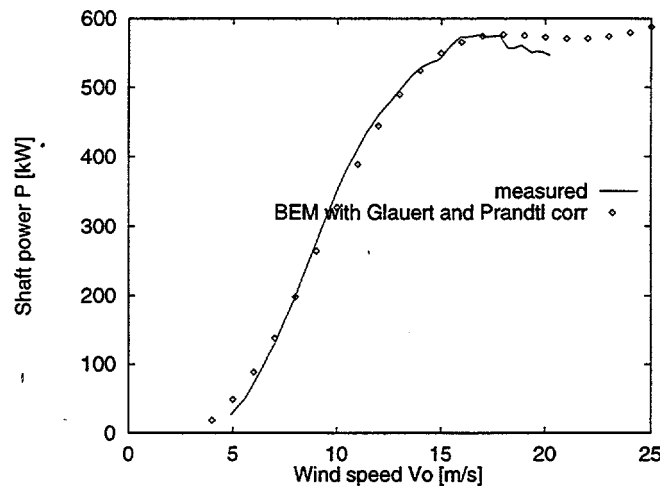


Figure 35: Comparison between computed and measured power curve, i.e. mechanical shaft power as function of the wind speed.

BEM method captures the measurements very well. It should be mentioned that the uncertainties on the measurements are big for the low wind speeds.

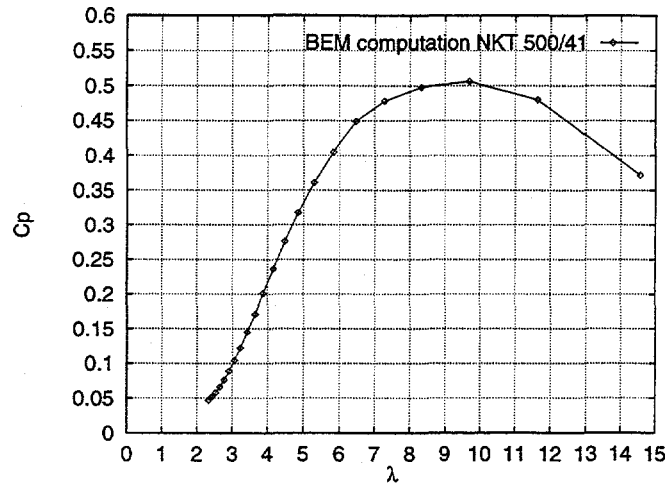


Figure 36: Power coefficient C_p as a function of the tip speed ratio $\lambda = \frac{\Omega R}{V_o}$.

The power curve is often shown in non-dimensional form as in figure 36 or 37. In figure 36 is seen that this particular wind turbine has a maximum efficiency of approximately $C_p = 0.5$ for a tip speed ratio $\lambda=10$. The advantage of plotting the power coefficient as a function of the inverse tip speed ratio is that λ^{-1} increases linearly with the wind speed V_o . If the turbine is erected at a site where the Weibull parameters are $k=1.9$ and $A=6.8$, which are typical values for a flat agricultural landscape, the annual energy output would be $1.12 \cdot 10^6 \text{ kWh}$ corresponding to the consumptions of approximately 300 households. It should be remembered that the Weibull parameters vary from site to site and has to be evaluated for each individual siting. The example shown here is for a stall regulated wind turbine (fixed pitch) but the BEM method can also be used to predict the power curve of a pitch regulated wind turbine. When the pitch is mentioned for an entire wind turbine it is referred to the pitch of the tip airfoil. A pitch regulated wind turbine normally operates at a fixed pitch until a certain nominal power is generated. For higher wind speeds the blades are pitched normally with the leading edge into the wind in order to keep this nominal power. Therefore the power curve of a pitch regulated wind turbine is absolutely flat after the nominal power has been reached. More runs are required with the BEM method to predict the power curve and the pitch setting for different wind speeds. First the power curve is computed with the fixed pitch θ_1 used for the small wind speeds. The procedure for computing a pitch regulated wind turbine is sketched in figure 38. At point A the nominal power is reached and it is necessary to change the pitch. More BEM calcu-

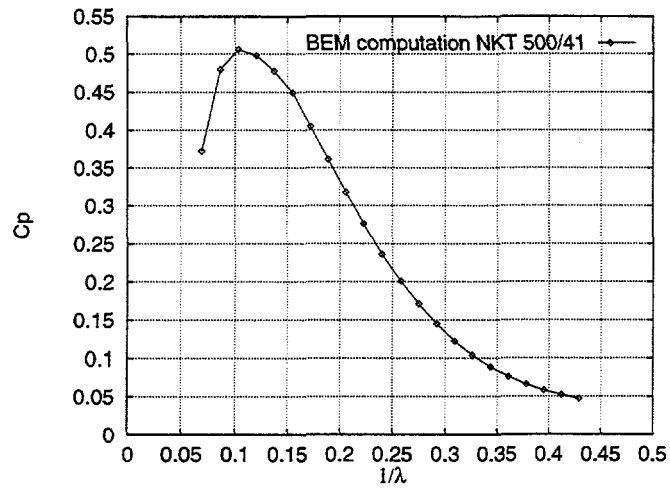


Figure 37: Power coefficient C_p as a function of the inverse tip speed ratio $\lambda^{-1} = \frac{V_0}{\Omega R}$.

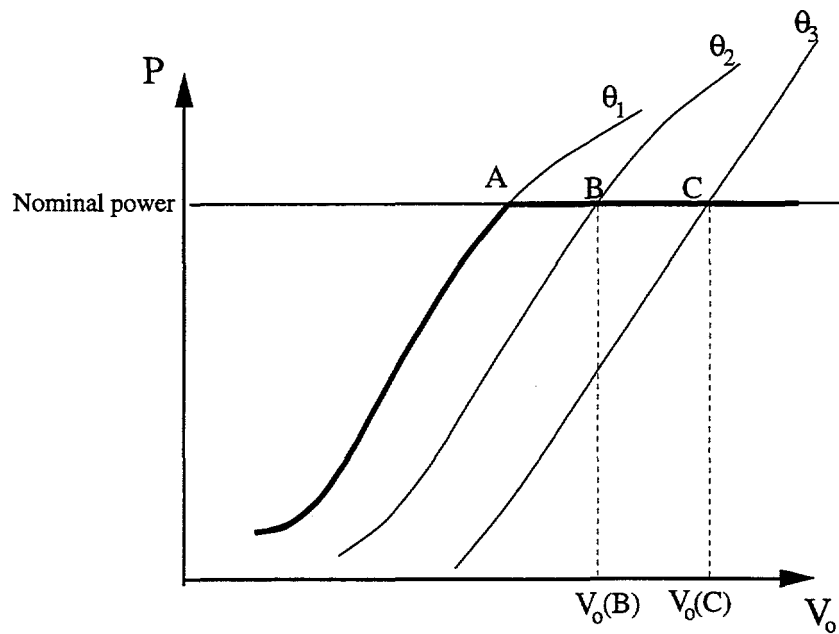


Figure 38: Sketch of a power curve for a pitch controlled wind turbine.

lations are made for a pitch of θ_2 and θ_3 . It is seen that for a wind speed of $V_o(B)$ the pitch must be changed to θ_2 . The BEM method as derived in these notes is stationary, so it is not possible to compute the transient from point A to point B and from point B to point C.

Optimization

After having derived all necessary equations to compute a given wind turbine one would like to use these to compute an optimum design. This is, however, not a trivial matter since one has to define what should be optimized. From an economical point of view one would seek a design that after a typical lifetime of 20 years has produced as much money as possible. To do this it is necessary to estimate a cost function for every component in the wind turbine and a maintenance cost. From a technical point of view one would like to design a wind turbine that for a given rotor diameter gives as many kWh/year as possible. If the turbine is sited at a spot where the wind speed V_o is constant in time it is obvious that one should optimize $C_p = P / \frac{1}{2} \rho A V_o^3$ at this wind speed. Of course such a place does not exist so it might be better to have a lower $C_{p,max}$ but with a "flatter" top as sketched in figure 39. As shown in the previous

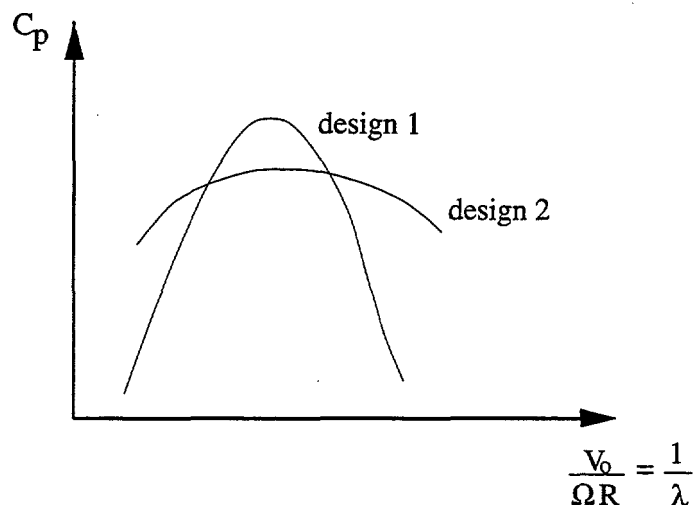


Figure 39: Two different designs. Design 1 has a high $C_{p,max}$ but C_p drops of quickly at different wind speeds. Design 2 has a lower $C_{p,max}$ but performs better over a range of wind speeds.

section the annual energy production is a combination of the wind distribution and the power curve. So the optimal design also depends on the actual siting. Of course it is imperative to ensure that an optimal design will survive the entire design period taking both extreme and fatigue loads into account. It is possible to compute the geometry of design 1 in figure 39 with the equations derived in this text. Such a design could be interesting for an airplane propeller, which is mainly operating at cruise speed. It could also be interesting

for a wind turbine with variable rotational speed. Such a machine could ideally by a control mechanism be kept at the optimum tip speed ratio $\lambda = \Omega R/V_0$ by varying the angular velocity Ω intelligently. First a good aerodynamic profile should be chosen. The profile should be relatively roughness insensitive and posses an acceptable stall characteristic. Also noise considerations might influence the choice of profile. A possible choise could be the NACA63-415 airfoil, which have proven to posses good stall characteristics on stall regulated wind turbines. Since we are now planning to operate in one point only it is specified that the effective angle of attack should have an optimum value along the entire span. An optimum value could be where the ratio between the lift to the drag is highest. From figure 40 can be seen that the NACA63-415

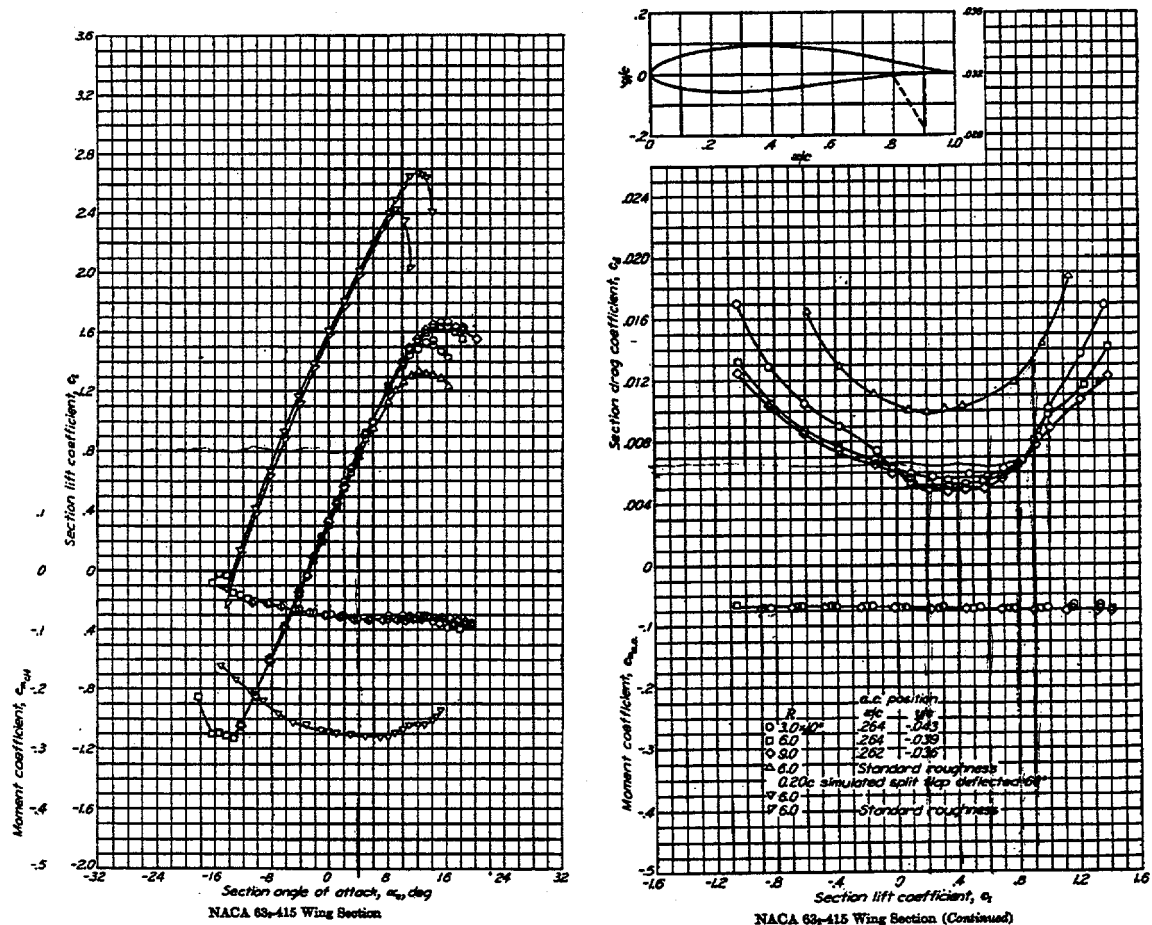


Figure 40: Profile data from [3] for the NACA63-415 profile.

profile at $Re=3 \cdot 10^6$ has a maximum value of C_l/C_d of approximately 120 at an angle of attack α of 4° . It is also seen that this maximum value drops to approximately 67 when standard roughness is added to the profile, but at the same optimum angle of attack of 4° . In the following example the values with roughness is used, i.e. $C_{l,opt}(4^\circ)=0.8$ and $C_{d,opt}(4^\circ)=0.012$. Further, the number of blades B is chosen to 3 and the design point to $\lambda=\Omega R/V_o=6$. Since an angle of attack of 4 is chosen in the design point the flow is attached to the blades and equations (48) and (54) are valid. Combining equations (48) and (54) yields an optimum relationship between x and a

$$16a^3 - 24a^2 + a(9 - 3x^2) - 1 + x^2 = 0. \quad (103)$$

The optimum value of a' is found using (54) and the optimum local pitch angle can then be computed as

$$\theta_{opt} = \phi - \alpha_{opt}, \quad (104)$$

since it is recalled that the flow angle ϕ is computed as

$$\phi = \text{atan} \frac{(1-a)V_o}{(1+a')\Omega r} = \text{atan} \frac{(1-a)}{(1+a')x}. \quad (105)$$

The optimum chord distribution is found from equation (77) using the optimum values for a and a'

$$c(x) = \frac{8\pi ax \sin^2(\phi)}{(1-a)BC_N\lambda}, \quad (106)$$

where

$$C_N = C_{l,opt} \cos \phi + C_{d,opt} \sin \phi. \quad (107)$$

For $\lambda=6$, $\alpha_{opt}=4$, $C_{l,opt}=0.8$, $C_{d,opt}=0.012$ and the number of blades $B=3$ the optimum chord and pitch distribution can now be computed and the solution is shown graphically on figures 41 and 42. Note, however, that in these simple expressions Prandtl's tip loss factor has been neglected. Taking this into account will change the optimum pitch and chord distribution close to the tip.

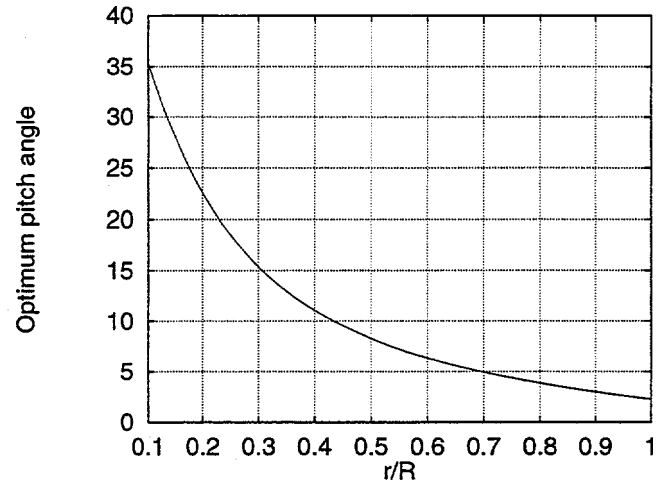


Figure 41: Optimum pitch distribution (neglecting Prandtl's tip loss factor) for $\lambda=6$, $\alpha_{opt}=4$, $C_{l,opt}=0.8$, $C_{d,opt}=0.012$ and $B=3$.

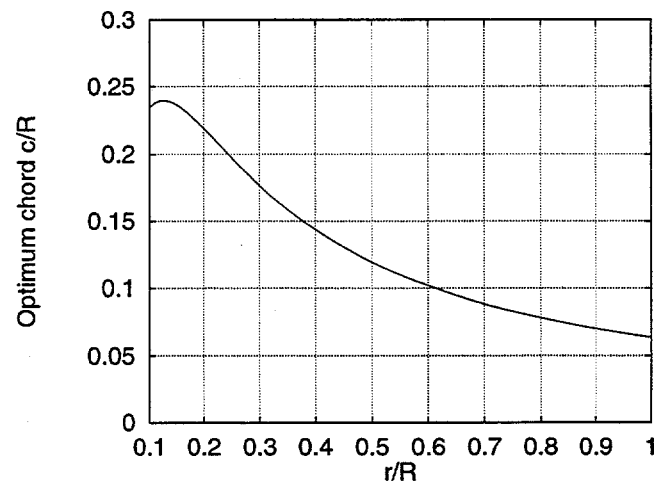


Figure 42: Optimum chord distribution (neglecting Prandtl's tip loss factor) for $\lambda=6$, $\alpha_{opt}=4$, $C_{l,opt}=0.8$, $C_{d,opt}=0.012$ and $B=3$.

Limitations

The final section in this note concerns some of the major limitations and shortcomings of the classical BEM method. As has been shown in the previous sections, good results depend on possessing reliable and tested airfoil data. Blade and wind turbine manufacturers have after a long experience obtained good data for the profiles they use. But if they want to build a blade with new airfoils they have to be very careful. One of the most profound shortcoming of the basic method, however, is that only stationary solutions can be obtained. In reality the wind seen by a wind turbine is not stationary due to turbulence, wind shear and influence from the tower as illustrated in figure 43. The constantly changing local angles of attack change the loads and the speed

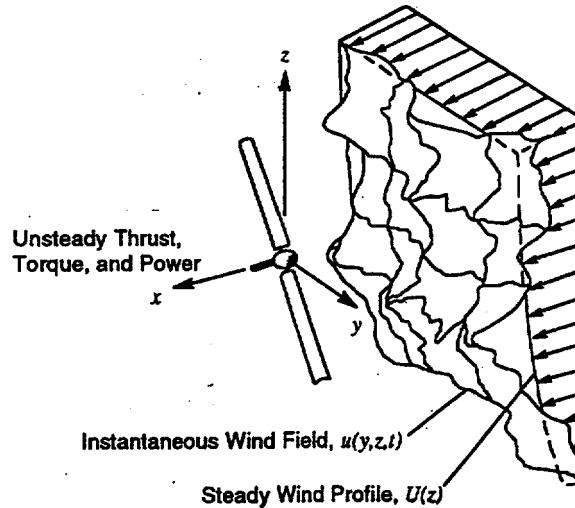


Figure 43: A schematic drawing of a real wind field. The figure is borrowed from [10].

vortices in the wake. To simulate this it is necessary to extend the simple BEM method with a time constant taking into account that it takes a certain time T to go from one stationary solution to another. If the stationary solutions at time t and $t + \Delta t$ is computed by the stationary BEM method as e.g. $a(t)$ and $a(t + \Delta t)$ then the actual solution at $t + \Delta t$ is found as

$$a(t + \Delta t) = a(t) + \frac{\Delta t}{T}(a(t + \Delta t) - a(t)), \quad (108)$$

where the time increment Δt is smaller than the time constant T . It is noted that the time constant T depends on the mean wind speed, since at high wind speeds the shed vortices from changing the loads are quickly convected downstream in the wake and the induced velocities respond faster to changes in the loading. It is also necessary to have a structural model of the wind turbine since the blades are responding elastically to the changing loads. In the flapwise direction, i.e. in an out of the rotorplane the blades are relatively soft and prone to oscillate. Modern wind turbine blades are now reaching a size where also edgewise (lead-lag) oscillations may occur, that is oscillations within the rotorplane. In figure 44 the velocities seen by a moving airfoil section is drawn. In figure 44 a situation is drawn where the profile is moving

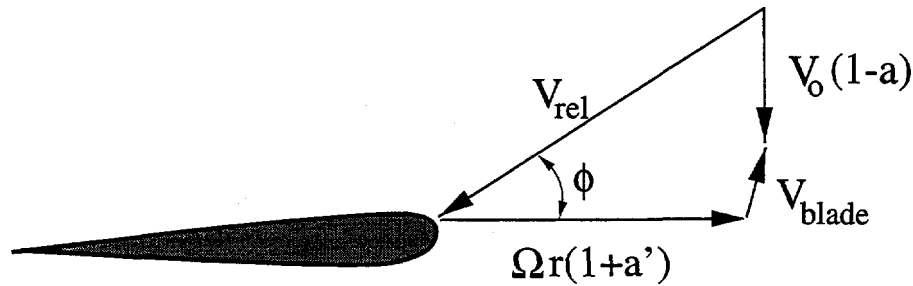


Figure 44: *Moving airfoil section.*

upstream and slightly forward and it is seen that this increases the angle of attack. The opposite is the case when the profile moves downstream some time later, so the angle of attack varies not only from the turbulence but also from the oscillation of the airfoil itself. If the angle of attack of an airfoil is changed sinusoidally in a windtunnel by rotating or heaving the airfoil about an equilibrium position the lift will not follow the static curve due to hysteresis in the boundary layer. A closed loop around the stationary value is observed as shown in figure 45 and this phenomenon is called dynamic stall. The shape of the curve depends on the frequency, the amplitude, the mean angle of attack and the Reynolds number. Several engineering models exist to predict the shape of the dynamic stall loops like the ONERA, Beddoes or Gormont models. A code which include a structural model, a model for the wake expansion (time constant), a dynamic stall model and which is coupled to a BEM method for the aerodynamic loads is called an Aeroelastic code. To use such a code one must first compute, based on an assumed turbulence intensity, a turbulent wind field of typically 10 minutes duration for each mean wind speed in which the turbine is operating. The loads on the turbine is then computed using the aeroelastic code for each wind speed. Using the Weibull wind distribution

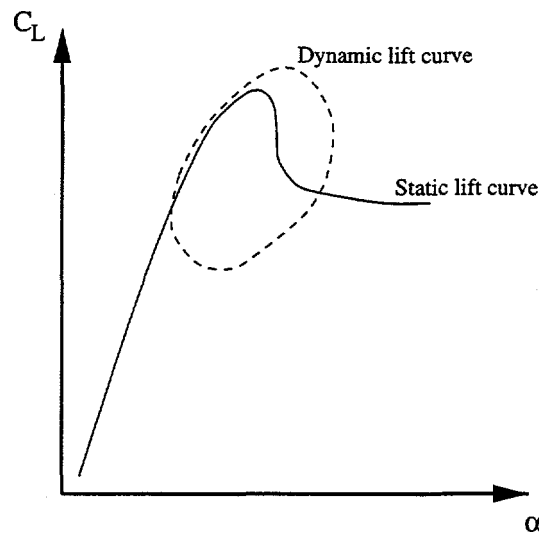


Figure 45: *Dynamic stall loop.*

on a given site one can estimate the load spectrum for the entire lifetime of the turbine, i.e. the actual number of cycles with a given mean load and loadwith. From this load matrix a fatigue lifetime analyses can be performed. A typical output from an aeroelastic computation using FLEX4 is seen in figure 46. Another major limitation of the standard BEM method is that it is only possible to compute the static loads when the turbine is perfectly aligned with the wind, i.e. where a vector normal to the rotorplane is parallel to the wind vector. This situation is called zero yaw, where the yaw angle is defined as the angle between the rotor normal vector and the wind speed vector. It is possible to make some corrections to the BEM model to compute cases with a yaw angle different from zero. In such a case the angle of attack will vary with a frequency corresponding to the frequency of the rotation of the blades and the amplitudes may be quite large. It is important to be able to compute such cases for a complete lifetime analysis and such models are therefore included in all aeroelastic codes.

500/37, V=11, Ti=0.1, Ktors=2.5E7

08.05.92 11:36

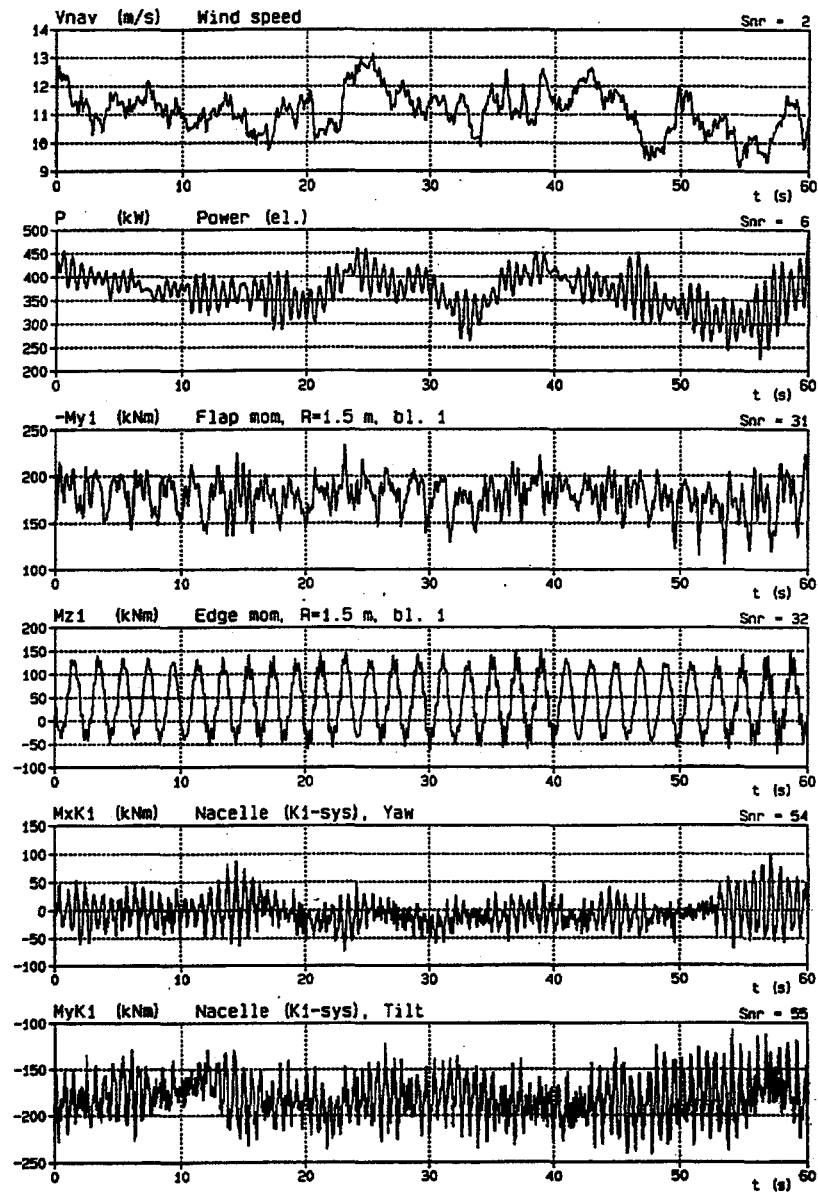


Figure 46: Example of computed loads using FLEX4 for a mean speed of 11m/s.

Final Remarks

It is the hope of the author that the notes will impart a basic understanding of the mechanisms behind the production of forces on a wind turbine. Even though aeroelastic codes, including a standard Blade Element Momentum method, can be bought, it is considered important that the theory behind this method and its limitations is understood. The aerodynamics of a wind turbine is important, but building a wind turbine is a multi disciplinary task since it requires knowledge of meteorology, atmospheric turbulence, fluid mechanics, structural dynamics, generators, electrical grid connections, gear boxes, hydraulics, foundations, economics and so on. The author wants to wish good luck to anybody who is willing to persue any of these tasks in order to harvest more efficiently the vast resources contained in the wind.

- [1] White, F.M., 'Viscous Fluid Flow', McGraw-Hill (1991).
- [2] Schlichting, H., 'Boundary-Layer Theory', McGraw-Hill (1968).
- [3] Abbot, H. and von Doenhoff, A.E., 'Theory of Wing Sections', Dover Publications (1959).
- [4] L.M.Milne-Thomson, 'Theoretical Aerodynamics', MacMillan (1952).
- [5] Schlichting and Truckenbrodt, 'Aerodynamik des Flugzeuges', Springer-Verlag (1959).
- [6] Wilson, R.E. and Lissaman, P.B.S., 'Applied Aerodynamics of Wind Power Machines', published by Oregon State University (1974).
- [7] Eggleston and Stoddard, 'Wind Turbine Engineering Design', Van Nostrand Reinhold Company (1987).
- [8] Glauert, H., 'Airplane Propellers' from Aerodynamic Theory, vol. 4, Division L edited by Durand W.F., Julius Springer, pp. 169-360, (1935).
- [9] Øye, S., 'FIX Dynamisk, Aeroelastisk Beregning af Vindmøllevinge' (in danish), Department of Fluid Mechanics DTU, AFM83-08, (1983).
- [10] Spera, D.A., 'Wind Turbine Technology', ASME Press (1994).
- [11] Troen, I. and Petersen E.L., 'European Wind Atlas', Risø National Laboratory (1989).
- [12] Dansk Ingeniørforenings og ingeniør-sammenslutningens Norm for, 'Last og sikkerhed for vindmøllekonstruktioner', DS 472, maj 1992. (Danish standard)
- [13] Paulsen, U.S., 'Konceptundersøgelse Nordtank NTK 500/41 Strukturelle laster' (In danish), Risø-I-936(DA), 1995.
- [13] Øye, S., 'FLEX4 Simulation of Wind Turbine Dynamics' from proceedings of 28th IEA Meeting of Experts, State of the Art of Aeroelastic Codes for Wind Turbine Calculations', 1996.